Historical Multidecadal Variability of Intraseasonal Features of Sahel Rainfall in CMIP6 models and observations

Pablo Fernández[1] , Juliette Mignot[1] , Alessandra Giannini[2] , Elsa Mohino[3] , Guillaume Gastineau[1] , Frédéric Hourdin[2]

[1] *Laboratoire d'Océanographie et du Climat: Expérimentations et Approches Numériques, Institut Pierre-Simon Laplace, Sorbonne Université/CNRS/IRD/MNHN, Paris, France,* [2] *Laboratoire de Météorologie Dynamique/IPSL, Ecole Normale Supérieure, Université PSL, Sorbonne Université, École Polytechnique, IP Paris, CNRS, Paris, France,* [3] *Physics of the Earth and Astrophysics Department, Complutense University of Madrid, 28040 Madrid, Spain.*

Corresponding author: Pablo Fernández, pablo.fernandez-fernandez@locean.ipsl.fr

ABSTRACT: We compare observations and the historical simulation large ensembles of three CMIP6 models to understand the role that external forcings and internal variability may have played in modulating the frequency and intensity of daily rainfall, and the duration of the rainy season in the Sahel. We compare three periods: [1950-1970], [1970-1990] and [1994-2014]. The results show that the anomalously wet [1950-1970] and [1994-2014] periods are characterized by more extreme rainfall days and longer monsoon seasons than the drier [1970-1990] period. While in the [1950-1970] to [1970-1990] transition the internal variability plays a dominant role in modifying Sahel intraseasonal rainfall features, the [1970-1990] to [1994-2014] recent recovery shows a stronger impact of the total forced signal. Furthermore, we explore the contributions of anthropogenic aerosols (AAs) and greenhouse gases (GHGs) in both transitions. An increase in European and North American AA emissions between [1950-1970] and [1970-1990] reduces the frequency of extreme and heavy rainfall days and shortens the wet season. The shift of AA emissions from North America and Europe to Asia between [1970-1990] and [1994-2014] has the opposite effect. In contrast, an increase in GHG concentrations in the atmosphere increases the frequency of extreme rainfall days and delays the end of the wet season, but does not affect the frequency of heavy days. We note that the effects of AA and GHG almost cancel each other out in the [1950-1970] to [1970-1990] transition, while they add up in the [1970-1990] to [1994-2014] recovery.

1. Introduction

The Sahel is a semi-arid region in West Africa located between Senegal and Sudan, limited to the north by the Sahara Desert and to the south by savannah. Most of the rainfall in this region occurs between June and September and is associated with the mature phase of the West African monsoon (WAM) (Thorncroft et al. 2011; Biasutti 2019). Sahelian rainfall experiences significant variability at time scales from intraseasonal (Sultan et al. 2003) to interannual (Losada et al. 2010; Nicholson 2013) and decadal (Giannini et al. 2003). The decadal variability of the seasonal amount of rain is very high, representing approximately 50% of the total year-to-year rainfall variance (Kitoh et al. 2020). In particular, a very wet period took place in the 1950s and 1960s, followed by a drier period in the 1970s and 1980s, and by a partial recovery at the beginning of the 21^{st} century (Nicholson 1983; Lebel and Ali 2009; Berntell et al. 2018).

Most of the studies performed to understand this decadal to multidecadal variability focus on total Sahel precipitation accumulated during the wet season and its relation to slowly evolving climate system subcomponents, notably sea surface temperature (SST, Folland et al. 1986; Giannini et al. 2003; Mohino et al. 2011; Villamayor et al. 2018; Hirasawa et al. 2020, 2022; Zhang et al. 2022; Guilbert et al. 2024). In particular, Atlantic Multidecadal Variability (AMV) has received special attention because it explains an important fraction of the variance of Sahel precipitation (Mohino et al. 2011; Rodríguez-Fonseca et al. 2011). Although the AMV was originally thought to be an internal mode of variability of the climate system (Knight et al. 2005; Knight 2009; Ting et al. 2009, 2011; Zhang et al. 2019), some studies have found increasing evidence of the importance of external forcings in its generation (Rotstayn and Lohmann 2002; Biasutti and Giannini 2006; Kawase et al. 2010; Ackerley et al. 2011; Biasutti 2011; Booth et al. 2012; Clement et al. 2015; Bellomo et al. 2018; Mann et al. 2021; Klavans et al. 2022) and thereby the modulation of Sahel rainfall (Hirasawa et al. 2020, 2022).

Among the external forcings, concentrations of greenhouse gases (GHGs) and anthropogenic aerosols (AAs) have significantly changed over the last century and have been shown to strongly impact Sahel rainfall (Monerie et al. 2022). On the one hand, the increase in European and North American AA emissions between the 1950s and the 1980s acted to cool the North Atlantic, reducing moisture supply towards the Sahel and triggering a southward displacement of the Intertropical Convergence Zone (ITCZ, Booth et al. 2012; Hirasawa et al. 2020). On the other hand, the partial

precipitation recovery at the beginning of the 21^{st} century has been found to be a combination of increased GHG concentrations (Dong and Sutton 2015) and decreased North American and European AA emissions (Hirasawa et al. 2020). However, the uncertainty in climate simulations in the implementation of and response to these forcings is large. For example, the effect of AAs is stronger in the Coupled Model Intercomparison Project Phase 6 (CMIP6) than in CMIP5, presumably because the AA forcing is also larger (Fyfe et al. 2021) and the fact that more CMIP6 models include aerosol-cloud interactions (Menary et al. 2020). This introduces another source of uncertainty when evaluating Sahel precipitation response to different forcings. Hence, the relative importance of the different contributions from each external forcing in Sahel rainfall multidecadal modulations remains an open research question.

All the studies cited above refer to Sahel total precipitation accumulated during the wet season. However, the multidecadal variability of Sahel intraseasonal rainfall characteristics (e.g., onset, demise and duration of the wet season, frequency and intensity of and extreme rainfall days) over the historical period and their linkage to external forcings and internal variability have received less attention in the literature. One reason may be that its evaluation requires long time series (of several decades) of daily precipitation data in a region with a sparse coverage of *in-situ* stations.

Yet, Le Barbé et al. (2002) showed that the rainfall deficit observed in the 1970s and 1980s was linked to a decrease in the frequency of rainfall events rather than their intensity. More recent literature shows that the observed Sahel rainfall recovery in recent decades is reflected in more extreme rainfall events (Panthou et al. 2014; Sanogo et al. 2015; Taylor et al. 2017; Sanogo et al. 2022; Chagnaud et al. 2022) resulting in an enhanced hydrological cycle. However, the recovery is not uniform over the Sahel: the eastern and central Sahel are experiencing a recovery while the west remains dry (Lebel and Ali 2009; Panthou et al. 2018; Blanchet et al. 2018).

In addition, Diakhaté et al. (2019) used satellite and gauge-based observations with reanalysis to assess the interannual variability of Sahel moderate, heavy and extreme rainfall events in relation with SST anomalies of different ocean basins in the period 1981-2016. They found that Sahel extreme and heavy precipitation events become more frequent during La Niña years and a warmer-than-average Mediterranean Sea, while moderate rainfall interannual variability seems to be primarily associated with temperature anomalies in the tropical North Atlantic and the Mediterranean Sea. Other studies such as Salack et al. (2014) found an increase of dry spells over

the Sahel when the global tropics are warmer. Based on daily gauge records in the 1918-2000 period, Badji et al. (2022) suggested that the AMV-like SST anomalies in the North Atlantic could modify Senegal rainfall intraseasonal characteristics including extreme rainfall days at decadal timescales. However, the recent decoupling in the precipitation trend between the eastern and the western Sahel (Lebel and Ali 2009) hinders the extrapolation of these results to the entire Sahel.

All these observation-based studies are limited by the short time series of daily data and/or their sparse coverage. Regarding models, Sow et al. (2025) characterized the total Sahel precipitation by means of the frequency and intensity of rainy days. They showed using various CMIP6 coupled model historical simulations that the recent recovery is characterized by more intense rain events which also become more frequent. Similar conclusions were drawn by Chagnaud et al. (2023), who in addition highlighted the dominant role of increased GHG atmospheric concentrations in rainfall intensification in the eastern Sahel. However, they concluded that while climate simulations seem to correctly reproduce rainfall occurrences in the last 30 years, they fail to capture the observed trend of longer extreme dry spells. Finally, other studies assessing Sahel intraseasonal characteristics consist of targeted experiments focusing only on a given pattern (such as the AMV in Mohino et al. 2024) and not the full potential sources of their multidecadal variability.

In this context, this paper aims to study a wider range of intraseasonal features of Sahel rainfall than the previous modeling literature by including the different rainy day categories and the wet season timing. In particular, we propose to answer the following questions: How do intraseasonal features of Sahel rainfall evolve during the historical period at the multidecadal time scale in models? In particular, how do the timing of the wet season and the frequency of extreme events covary? How does this compare with observations? What is the role of the external forcings against the internal variability in these modulations?

In responding to these questions, we provide a first comparison of (Eyring et al. 2016) large ensembles of historical simulations and of dedicated simulations from the Detection-Attribution Model Intercomparison Project (DAMIP, Gillett et al. 2016) to gauge-based observations. The article is structured as follows. Section 2 describes the different datasets used, section 3 presents the methodology used to analyze these data. Section 4 contains the main results of the paper and Section 5 explains the main conclusions and perspectives.

2. Data

a. CMIP6 models

We make use of three types of simulations carried out in the framework of CMIP6 (Eyring et al. 2016): preindustrial control, historical and Detection-Attribution Model Intercomparison Project (DAMIP) (Gillett et al. 2016). The historical simulations are forced by the time-varying observed external anthropogenic (aerosols, greenhouse gases, stratospheric ozone and land use changes) and natural (solar radiation and volcanic aerosols) forcings over the period spanning from 1850 to 2014. For each model, the ensemble mean isolates the forced signal. The larger the number of members, the more accurate the estimation of the forced response is (Kay et al. 2015). In our study, we use the large-ensemble of historical simulations of three CMIP6 models. These models were chosen because they each provide an ensemble of more than 30 members. Detailed information is provided in Table 1.

DAMIP simulations keep the setup of historical simulations but are only constrained by one time-varying forcing while the others are maintained to the 1850 levels (Gillett et al. 2016). Therefore, they enable the disentanglement of the effects of the single forcings to the total forced signal obtained from the historical simulation ensemble mean, if sufficient members are provided, and assuming that these effects add up. In this study, we only make use of hist-aer and hist-GHG from the IPSL-CM6A-LR model that are constrained by AAs and GHGs respectively. hist-aer has 25 members and hist-GHG 14 which contain the daily precipitation data required to compute Sahel intraseasonal rainfall features.

Finally, the preindustrial control simulations (piControl) are based on fully coupled models forced with non-evolving preindustrial conditions representative of the 1850 reference year. These simulations allow to characterize the internal multidecadal variations only due to interactions between climate system components (in the absence of variation in external forcings). In this study, we only make use of the IPSL-CM6A-LR piControl simulation (Boucher et al. 2020). It is 2000 years long and provides precipitation data at a monthly resolution.

In addition to these three types of coupled simulations, we also use Atmospheric Model Intercomparison Project (AMIP)-type IPSL-CM6A-LR simulations to further analyze the role of SST Sahel precipitation multidecadal variability. Here, the atmospheric component of the IPSL-

TABLE 1. Information on the CMIP6 models used in this study.

Model name	Atmospheric resolution (lon × lat)	# members of the historical simulation	Reference
IPSL-CM6A-LR	2.5° × 1.27°	32	Boucher et al. (2020)
CESM2	1.25° × 0.9°	84	Danabasoglu et al. (2020)
MIROC6	1.4° × 1.4°	50	Tatebe et al. (2019)

CM6A-LR coupled model (LMDZ) is forced with observed SST. We use a monthly 20-member AMIP ensemble which has the same spatial resolution as its historical coupled counterpart and covers the 1958-2014 period.

b. Observations

We analyze the Rainfall Estimate on a Gridded Network all stations version 1 (REGEN) dataset (Contractor et al. 2020) is utilized. REGEN is a daily rainfall dataset based on gridded rain gauges that includes all stations from the Global Historical Climate Network (GHCN-Daily). It spans from 1950 to 2016 at 1° horizontal resolution. We selected this dataset among other gauge-derived products since it was the only one among the datasets in Sanogo et al. (2022) presenting the daily values required to compute the intraseasonal rainfall characteristics over a sufficiently long period. In addition, it has been shown to properly reproduce extreme precipitation event properties over the Sahel with reasonable skill (Sanogo et al. 2022). We compare it with the model output of the historical simulation throughout the manuscript.

In order to add robustness in the comparison between model and observations we also use the monthly Climate Research Unit, version 4.01 dataset (CRU TS 4.01, Harris et al. 2020). Note that in CRU only monthly data are available. Thus, we are only able to validate total precipitation and not Sahel intraseasonal characteristics with it. CRU data are available between 1901 and 2016 at a 0.5° horizontal resolution.

3. Methodology

a. Intraseasonal Features in Sahel Rainfall

We define a day to be wet or rainy when the total amount of rainfall exceeds 1 mm (Hartmann et al. 2013). This definition has been widely applied to observations since it allows to account for

instrumental uncertainty. Concerning models, some authors have proposed an adaptable threshold to account for the higher share of total annual rainfall produced by small daily rainfall amounts (Chagnaud et al. 2023) in climate models; while others always consider 1 mm (Mohino et al. 2024; Sow et al. 2025). In this article, we decide to keep 1 mm irrespective of observations or models for simplicity. We have checked that the adaptable definition of Chagnaud et al. (2023) does not significantly modify the conclusions of this study.

SI ?

We classify rainy days based on percentile thresholds into extreme (>95^{th}), heavy (>75^{th} and <95^{th}) and moderate (<75^{th}). Thresholds are calculated over each Sahel grid point separately using rainy days that belong to the May-to-October (MJJASO) season in the 1950-2014 period. For each specific type of simulation, all members are taken into account to calculate the threshold. We select this long season since it contains the mature phase of the West African monsoon, when rainfall is well developed over the Sahel (Thorncroft et al. 2011) as well as extreme precipitation events which might occur outside the core of the rainy season. We then count the number of times the threshold-based criterion is fulfilled at each grid point per MJJASO season. This methodology produces three frequency indices (with dimensions latitude × longitude) per MJJASO season: n_e, n_h and n_m standing respectively for the frequency of extreme, heavy and moderate rainfall days.

n = nombre of days ?

Additionally, we compute the total rainfall accumulated per MJJASO season associated with each rainy day category (i.e. extreme, heavy and moderate). We then divide it by the number of rainy days of the corresponding category in the MJJASO season to obtain the rainfall intensity (WMO 2009; Zhang and Delworth 2006; Herold et al. 2016) for each category of rainy day, which we denote as I_e, I_h and I_m for extreme, heavy and moderate rainfall days respectively.

We finally relate the total precipitation accumulated over each MJJASO season, expressed as a mean value per day (p; in mm d^{-1}) to the number of wet days of each category and their intensity, allowing for P_{nr} to capture the amount of rain (in mm) fallen during non-rainy days (<1 mm):

$$p = \frac{1}{N}\left(\underbrace{I_e\, n_e}_{\substack{\text{Precipitation linked to}\\ \text{extreme rainfall days}}} + \underbrace{I_h\, n_h}_{\substack{\text{Precipitation linked to}\\ \text{heavy rainfall days}}} + \underbrace{I_m\, n_m}_{\substack{\text{Precipitation linked to}\\ \text{moderate rainfall days}}} + \underbrace{P_{nr}}_{\substack{\text{Precipitation linked to}\\ \text{non-rainy days}}} \right), \qquad (1)$$

where N = 184 represents the number of days per MJJASO season. Changes in the total amount of rainfall between time periods, expressed as an average value per day (Δp) can then be related to changes in the frequency or intensity of each category by:

$$\Delta p = \frac{1}{N}(\Delta n_e\ \overline{I_e} + \Delta I_e\ \overline{n_e} + \Delta n_h\ \overline{I_h} + \Delta I_h\ \overline{n_h} + \Delta n_m\ \overline{I_m} + \Delta I_m\ \overline{n_m} + \underbrace{\Delta P_{nr} + \Delta n_e\ \Delta I_e + \Delta n_h\ \Delta I_h + \Delta n_m\ \Delta I_m}_{\text{Residual}}). \quad (2)$$

Here, ΔP_{nr} is the change in the amount of rain (in mm) fallen during non-rainy days (<1 mm) and $\overline{n_e}$, $\overline{n_h}$, $\overline{n_m}$, $\overline{I_e}$, $\overline{I_h}$ and $\overline{I_m}$ are the climatological frequency and intensity for each rainy day category. These climatological values are estimated in observations (in models) as the means in time (and across members) over the MJJASO seasons in 1950-2014. This decomposition allows to disentangle precipitation changes arising from variations in the frequency or intensity of each rainy day category. The terms $\frac{1}{N}\ \Delta n_e\ \overline{I_e}$, $\frac{1}{N}\ \Delta n_h\ \overline{I_h}$ and $\frac{1}{N}\ \Delta n_m\ \overline{I_m}$ represent precipitation changes explained by the variations in frequency of extreme, heavy and moderate rainfall days respectively. In turn, the terms $\frac{1}{N}\ \Delta I_e\ \overline{n_e}$, $\frac{1}{N}\ \Delta I_h\ \overline{n_h}$ and $\frac{1}{N}\ \Delta I_m\ \overline{n_m}$ define precipitation changes associated with modifications of the intensity of extreme, heavy and moderate rainfall days respectively. ΔP_{nr} together with the changes coming from the cross product anomalies are called the residual. As shown later, they are smaller than the rest of the terms. Eq. 2 extends the decomposition of total Sahel rainfall between the contributions of the frequency and intensity of rainy days presented in Sow et al. (2025) without specifying the rainy day category.

As explained in subsequent sections the periods considered in this article are [1950-1970] (humid), [1970-1990] (drought) and [1994-2014] (partial recovery). We assess the [1950-1970] − [1970-1990] and [1994-2014] − [1970-1990] differences, that is, humid minus dry.

We compute the onset, demise and duration of the monsoon season at each grid point following Liebmann et al. (2012). For each day of each calendar year, we first compute the daily rainfall anomaly as the difference between the rainfall of that day and the long-term climatological mean daily rainfall. As in Mohino et al. (2024), the long-term climatological mean daily rainfall is computed taking into account all available years in observations and all years and ensemble members in the models. These daily anomalies are then cumulated from the 1^{st} of January to a

J'ai un peu du mal à comprendre cette description des dates de onset et demise

given calendar day. The dates for the minimum and the maximum of the daily cumulative rainfall anomaly provide the onset and demise timing respectively of the rainy season each year. The duration of the season is computed as the difference between the demise and the onset. We also tested other methods to compute the timing of the wet season (Marteau 2010; Sivakumar 1988). Instead of calculating the cumulative rainfall anomaly, these methods are based on the presence of sequences of consecutive wet days, whose cumulated rainfall exceeds a certain threshold, followed (or not) by a sequence of several non-rainy days. Since they yield similar results to Liebmann et al. (2012)'s, we do not show them in this study.

Finally, in order to provide an insight of the covariability between the frequency of extreme rainfall days and the duration of the rainy season between periods of study, we compute the ~~concentration~~ percentage of extreme rainfall days (r, ~~expressed as a percentage~~). For simplicity, here we focus on the meridional variations of extreme rainfall day concentration within the latitude-varying rainy season length. The possible east-west asymmetries are left for future research. For a given latitude and accounting for all Sahel longitudes, we count the number of times a certain day of the year belongs to the extreme rainfall day category (N_e). In models, we count along all members and longitudes and in observations only along longitudes. We then divide this quantity by the number of longitude locations in the Sahel box (n_{lon}) and the duration of the rainy season at the given latitude (L). This operation yields the ratio between the number of extreme rainfall days and the length of the rainy season at each latitude, here so-called concentration of extreme rainfall days.

$$r = \frac{N_e}{n_{lon} L} \tag{3}$$

All analyses in this article are performed over a "Sahel" box. The meridional limits of the Sahel are derived from the adaptable definition described in Ndiaye et al. (2022). This is motivated by the fact that the mean Sahel rainfall over MJJASO is abnormally shifted southward with respect to observations in the CMIP6 intercomparison exercise (Klutse et al. 2021). For each CMIP6 model (IPSL-CM6A-LR, CESM2 and MIROC6) historical simulation used here, we select the northernmost latitude where no more rain occurs (<0.5 mm d^{-1}) in MJJASO The southern limit corresponds to the latitude where the maximum of summer rainfall takes place. After this procedure, all three models show the same latitudinal limits: 8°N and 17°N. ~~In turn,~~ the latitudinal limits for REGEN and CRU are 10°-20°N. In both models and observations, we choose 17°W-25°E as the

"no more rain occurs" means what exactly ? Averaged raifnall < 0.5 mm/d over MJJASO?

longitudinal limits. In order not to consider locations over sea, where rainfall characteristics can be very different, we exclude from these boxes the grid points west of the line linking the locations 8°N-12.5°W and 12°N-17°W. The Sahel box considered for the models is represented in green in Fig. 4.

b. Statistical Significance

To test whether the change in a given quantity is statistically significant, we apply the parametric *t*-test for independent samples with different variances, assuming a Gaussian distribution (Wilks 2019). In models, we do not treat each year of an ensemble member as an independent realization. Instead, we take the average over the years of each period of study and consider each member as an independent realization as in Mohino et al. (2024).

Although our results are mainly based on comparison between models, we also attempt to validate precipitation changes with REGEN. In this case, we perform the *t*-test in REGEN along the time dimension. Despite the limited number of independent observations in REGEN between the periods compared, we chose this parametric test instead of a non-parametric Montecarlo test. The short time span of the observations (1950-2014) would indeed have restricted the random selection of a sufficiently large number of 21-year long non-overlapping two-period samples to estimate the statistical significance and thereby biased the results. We are aware that the *t*-tests performed in models and observations are not completely equivalent. Yet, this is an optimized pragmatic choice due to data availability.

4. Results

a. Multidecadal Variations of Sahel-averaged Total Precipitation Change

Fig. 1a represents the time series of the Sahel-averaged May-to-October (MJJASO) anomaly from 1901 to 2014. The precipitation time series has been low-pass filtered with a 30-year cutoff Butterworth filter, in order to isolate the multidecadal variability. REGEN and CRU display a humid period in the 1950s and 1960s followed by a drier 1970s and 1980s in agreement with previous studies (Nicholson 1983; Lebel and Ali 2009; Berntell et al. 2018). In the last decades, MJJASO precipitation has slightly increased although not to the 1950s levels. In addition, the observational datasets differ after the mid-2000s : while CRU precipitation grows until the mid

2000s and then seems to stabilize, REGEN displays a precipitation peak before 2000 and then slightly decreases. The precipitation minimum in both of them lies around 1982. Based on the evolution of the observed Sahel precipitation, we define three study periods with different total precipitation amounts delimited with the vertical dashed lines. Period 1 is [1950-1970] and is characterized by anomalously humid conditions, period 2 is [1970-1990] and represents the anomalous drought. Finally, [1994-2014] is period 3, and constitutes the partial precipitation recovery.

The thick black line represents the IPSL-CM6A-LR mean Sahel precipitation anomaly time series. There is a slight decline in precipitation from the late-1950s to the mid-1970s providing a less pronounced drought than in REGEN and CRU. Mean MJJASO precipitation then starts to increase around 1977 monotonically until it stabilizes in the late 2000s. The start of the precipitation increase in the 1980s occurs before observations. Note that the absence of a strong precipitation reduction between [1950-1970] and [1970-1990] in the ensemble mean time series is linked to the fact that each individual member (thin gray, purple, green and orange lines) shows a different phase of multidecadal variability. Although one cannot exclude at this stage that external forcings and their response may be subject to biases in the model, this suggests that internal variability is an important contributor to the total precipitation signal in the IPSL-CM6A-LR model during this transition. This conclusion does not necessarily imply that individual forcings such as GHGs and AAs are not acting. Indeed, their opposing effect on Sahel total precipitation in the recent recovery has been documented by Monerie et al. (2022) and the same analysis performed on the CMIP5 counterpart of IPSL-CM6A-LR captures a more pronounced precipitation decrease from 1950 onward, suggesting that individual forcings balance out differently (Giannini and Kaplan 2019). We come back to this point in following sections regarding precipitation extremes. On the contrary, all individual members agree on the increasing precipitation tendency between the [1970-1990] and [1994-2014] periods, suggesting a clearer role of external forcings.

To check this, the boxplot in Fig. 1b shows the distribution of Sahel-averaged 30-year low-pass filtered precipitation differences using 5000 consecutive 21-year periods that were randomly selected in the piControl simulation of IPSL-CM6A-LR, which we use as an estimate of the internal variability range in the model. During the [1950-1970] to [1970-1990] transition, all but two members show precipitation changes which could be explained solely by internal variability.

Observartions sur (b) ?
Montrer les extrêmes sur la boites au milieu. 2% de points en dehors. Ca fait quand même 0.02*5000 = 100 cas !

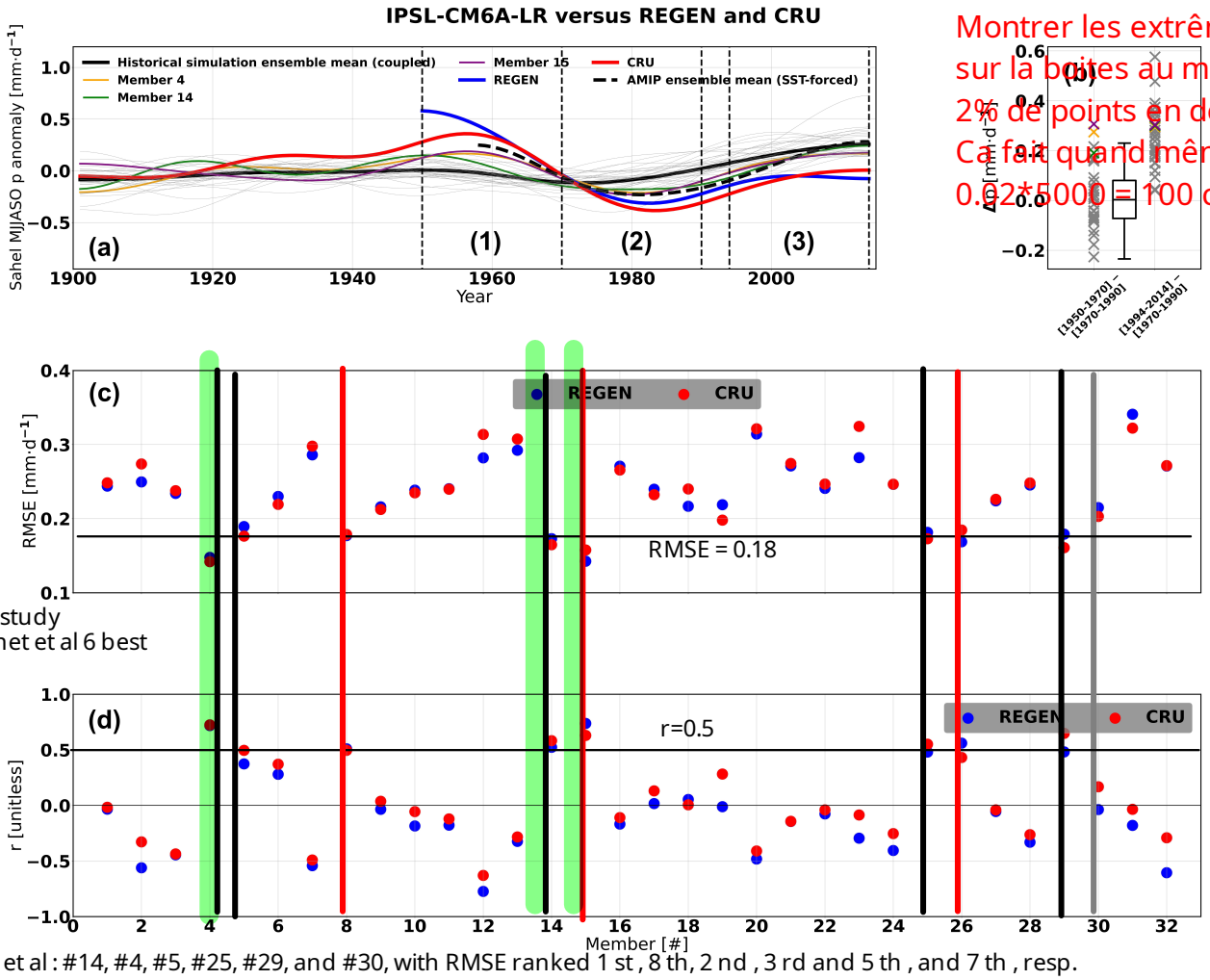

Bonnet et al : #14, #4, #5, #25, #29, and #30, with RMSE ranked 1 st , 8 th, 2 nd , 3 rd and 5 th , and 7 th , resp. These members are characterized by a strengthening of the AMOC until the 1940s followed by a decline, although member #30 shows a different evolution from the other members until the 1920s (Fig. 2b).

FIG. 1. (a) Time series of Sahel averaged MJJASO low-pass filtered mean precipitation of REGEN (blue), CRU (red), the IPSL-CM6A-LR 32-member historical simulation ensemble mean (black), individual members (gray), the three-most similar members (orange, green and purple) to REGEN and CRU in terms of RMSE and correlation coefficient and the LMDZ AMIP (SST-forced) ensemble mean (thick dashed black). The three vertical dashed lines indicate the three periods considered in this article: (1) [1950-1970], (2) [1970-1990] and (3) [1994-2014]. (b) Boxplot of the differences between 5000 pairs of 21-year consecutive periods randomly selected in the IPSL-CM6A-LR piControl simulation. The lower and upper whiskers indicate the 1% and 99% percentiles of the distribution respectively and the horizontal line in the box represents the median. The markers located at the left (right) of the boxplot denote the [1970-1990] – [1950-1970] ([1994-2014] – [1970-1990]) Sahel-averaged MJJASO precipitation difference of each individual member (gray). The three-most similar members are color-coded as in panel (a). (c) RMSE between each individual IPSL-CM6A-LR historical simulation member (listed in the horizontal axis) and REGEN (blue dots) or CRU (red dots). (d) Like in (c) but for the Pearson correlation coefficient.

On the other hand, in the [1970-1990] to [1994-2014] transition, more than half of the members lie outside the internal variability distribution, confirming the more important role of the forced signal in this transition.

To evaluate the representation of the multidecadal evolution of Sahel precipitation in the IPSL-CM6A-LR model, the root-mean square error (RMSE) and the Pearson correlation coefficient are calculated between the reference time series (REGEN and CRU) and each model member as in Bonnet et al. (2021a). They are displayed in Figs. 1c and d respectively. We retain the three members which present the lowest RMSE and the highest Pearson correlation coefficient considering REGEN and CRU results at the same time: members 4, 14 and 15. In particular, member 4 has the best representation of MJJASO precipitation modulations in comparison to both datasets (REGEN and CRU), with the lowest RMSE and the highest Pearson correlation coefficient. It is followed by members 14 and 15. We note that on the contrary, some members have a poor representation of MJJASO precipitation variations over the 1901-2014 period with large RMSE and a Pearson correlation coefficient close to zero (e.g. member 23). Assuming that the effect of external forcings is correctly captured by the model, these most similar members contain the effect of the forced signal and the closest-to-observations internal variability. Interestingly, these three members also match the longer-scale observed 1940-2016 trend in global air surface temperature and Atlantic Meridional Overturning Circulation (AMOC) variations, as shown in Fig. 2a of Bonnet et al. (2021b). This confirms a link between AMOC variability and precipitation in the Sahel (Zhang et al. 2021). The time series corresponding to these members are highlighted in colors orange, green and purple in Fig. 1a. Note that even these three members still show a weaker precipitation decrease between [1950-1970] and [1970-1990] and a stronger recovery between [1970-1990] and [1994-2014] than the observations. We will hereafter use these most similar members obtained with this analysis to evaluate the role of internal variability in changes in precipitation extremes by comparing the mean of the three with the ensemble mean.

cf. remarques document partagé

Finally, the AMIP simulation (LMDZ atmospheric model forced by observed SSTs) ensemble mean is shown with a thick black dashed line in Fig. 1a. The decrease in rainfall between [1950-1970] and [1970-1990] is better reproduced in AMIP than in the historical coupled simulation. This suggests that the IPSL-CM6A-LR coupled historical simulation misrepresents SST variations

over this period, either due to an underestimation of the SST response to the forcings (i.e. AAs or GHGs) or its multidecadal internal variability. We briefly return to this point in Section 5.

We conducted the same analysis for CESM2 and MIROC6. The results are shown respectively in Figs. A1 and A2 in Subsection a of the Appendix. The amplitude of the precipitation recovery seems to be well-captured in CESM2 and overestimated in MIROC6. Both models display an ensemble-mean precipitation decrease between [1950-1970] and [1970-1990], although it is weak as in IPSL-CM6A-LR and starts before 1950, unlike in IPSL-CM6A-LR.

b. Contributions of the Intraseasonal Rainfall Features to the Multidecadal Variations of Sahel-averaged Total Precipitation Change

The different terms of Eq. 2 are displayed in Fig. 2a. They represent the changes in the contributions to the total precipitation variation between two periods of study from the change in the frequency and intensity of extreme, heavy and moderate rainfall days.

Consistent with Fig. 1a, REGEN observations (bars) display a much stronger decrease in total precipitation (Δp) between [1950-1970] and [1970-1990] than recovery between [1970-1990] and [1994-2014]. In contrast, the three CMIP6 models (columns of markers within each cyan bar) generally show a stronger recent recovery, particularly in the ensemble mean, representing the forced signal (stars, see also Figs. 1a, A1a and A2a). This is a consistent feature across CMIP6 models (see Fig 3a of Ndiaye et al. 2022). Moreover, all individual members of the three models show positive values of Δp in the [1970-1990] to [1994-2014] transition. The three most similar members also display the same tendency, with values around the ensemble mean. In turn, the [1950-1970] to [1970-1990] transition shows weak ensemble mean Δp (below 0.1 mm d^{-1}, except for MIROC6). The three most similar members in this case present a larger Δp than the forced signal, among the largest of the respective ensemble of each model, suggesting an influence of internal variability. These results confirm what is shown in Figs. 1a, A1a and A2a.

Δp in both transitions is mainly explained by changes in the frequency of extreme and heavy rainfall days. The changes in the intensity of each rainy day category are always a second-order contributor when compared to their corresponding frequency counterpart.

In particular, the REGEN precipitation variation associated with the change in the frequency of extreme rainfall days ($\frac{1}{N}\Delta n_e \overline{I_e}$, second red bar in Fig. 2a) accounts for nearly half of the total Δp

Est-ce que si on multiplie toutes les pluies par un facteur constant, on n'obtient pas quelque chose d'analogue ?

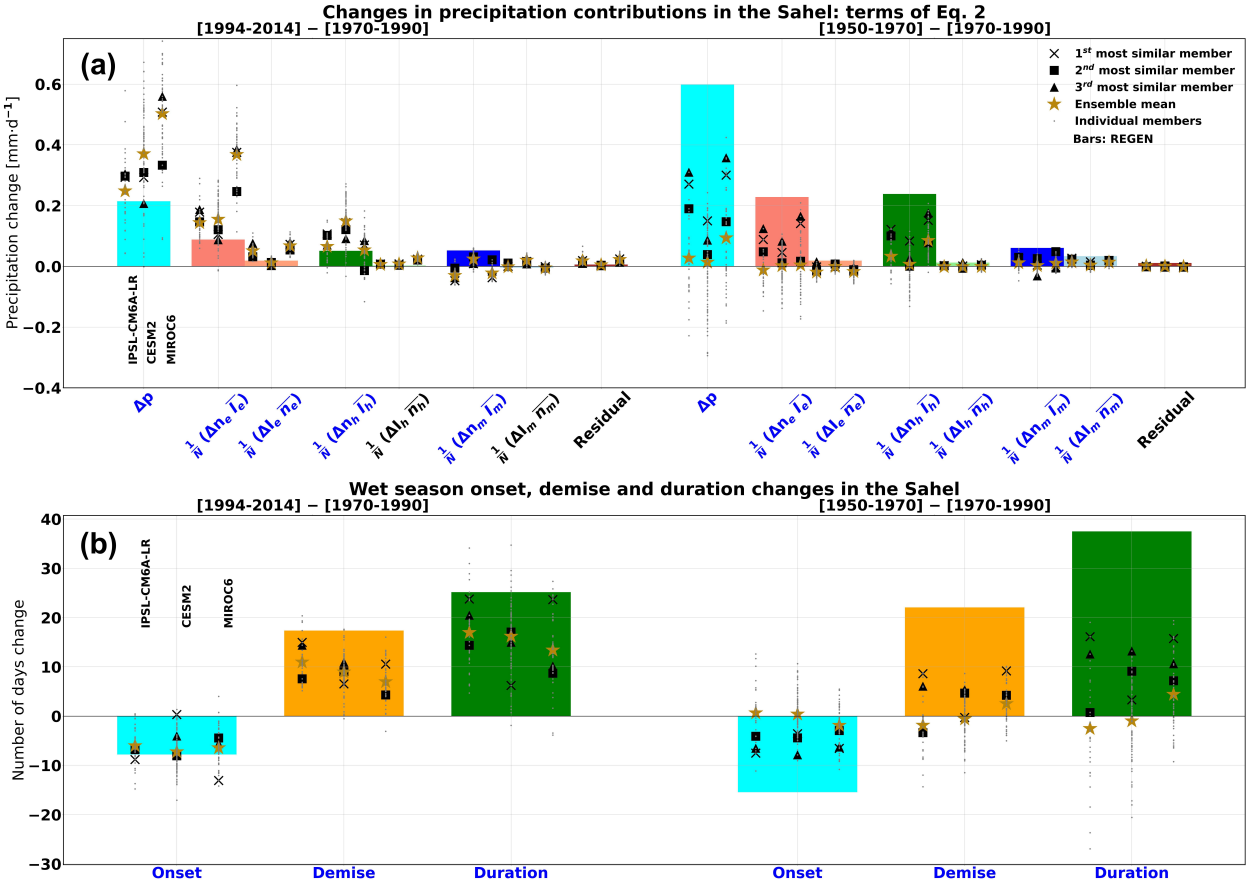

Fig. 2. (a) Sahel area-weighted mean variations between [1994-2014] and [1970-1990] (left) and [1950-1970] and [1970-1990] (right) of the different precipitation contributions in Eq 2. Bars represent the results for REGEN. The three groups of markers over each bar represent, from left to right the IPSL-CM6A-LR, CESM2 and MIROC6 historical simulation results. The gray dots depict the individual members and the black crosses, squares and triangles represent the first, second and third most similar members to observations respectively. In all cases, the golden stars stand for the ensemble mean. (b) Same as before but for the onset, demise and duration of the wet season computed following Liebmann et al. (2012). In both panels, blue labels indicate that the REGEN differences between periods (bars) are statistically significant after a two-sided t-test.

in [1970-1990] to [1994-2014] (0.09 out of 0.22 mm d^{-1}) and a third in [1950-1970] to [1970-1990] (0.23 out of 0.60 mm d^{-1}). In turn, models show that the precipitation recovery between [1970-1990] and [1994-2014] presents a strong $\frac{1}{N}\Delta n_e \overline{I_e}$ forced signal (especially MIROC6). All members except for one in CESM2 agree on this tendency across the three models. Conversely, the $\frac{1}{N}\Delta n_e \overline{I_e}$ forced signal between [1950-1970] and [1970-1990] is nearly zero for the ensemble

averages of three models and the three most similar members have positive values approaching the REGEN observations during this transition. Between [1970-1990] and [1994-2014] the three most similar members overestimate the REGEN $\frac{1}{N}\,\Delta n_e\overline{I_e}$ as they do with Δp. Finally, the contribution linked to the changes in the intensity of extreme rainfall days ($\frac{1}{N}\Delta I_e\overline{n_e}$) displays slightly positive values in IPSL-CM6A-LR and MIROC6 in the [1970-1990] to [1994-2014] transition, where all members agree. In both cases, this term represents less than 0.1 mm d^{-1}.

Another important contribution to Δp comes from the change in the frequency of heavy rainfall days ($\frac{1}{N}\Delta n_h\overline{I_h}$). In REGEN, this contribution is slightly positive during the recent recovery ($\sim$0.05 mm d^{-1}) and of the same magnitude as $\frac{1}{N}\Delta n_e\overline{I_e}$ in the [1950-1970] to [1970-1990] transition ($\sim$0.3 mm d^{-1}). In turn, the three models show a positive ensemble mean signal for this contribution in the [1970-1990] to [1994-2014] transition, which is especially strong in CESM2 ($\sim$0.18 mm d^{-1}). Again, in terms of $\frac{1}{N}\,\Delta n_h\overline{I_h}$ the forced signal and the most similar members present similar values in the recent recovery and tend to overestimate REGEN. Concerning the [1950-1970] to [1970-1990] transition, the $\frac{1}{N}\Delta n_h\overline{I_h}$ forced signal is weaker and the three most similar members generally lie closer to REGEN.

Except for the frequency of moderate rainfall events contribution in the recent recovery of REGEN related to its thresholds to separate between rainy day categories being higher than in models, the rest of the terms of Eq. 2 are smaller in magnitude. Thus, we hereafter focus our analysis on $\frac{1}{N}\Delta n_e\overline{I_e}$, $\frac{1}{N}\Delta I_e\overline{n_e}$ and $\frac{1}{N}\Delta n_h\overline{I_h}$. In the ensemble mean and individual model members, the sum of the three explains at least 90% of Δp between periods. In REGEN, their contribution is equal to 74%.

The multidecadal changes of the onset, demise and duration of the rainy season are shown in Fig 2b. In REGEN, the [1994-2014] period is characterized by an earlier onset ($\sim$8 d) and a later demise ($\sim$17 d) resulting in longer rainy seasons ($\sim$25 d) when compared to [1970-1990]. Consistently, all the three models show a forced signal and individual members signal with an early onset, a later demise and larger duration during the recovery period as compared to the dry one. This shows a dominance of the forcing, not counterbalanced by internal variability. In REGEN, the same changes are seen in the [1950-1970] to [1970-1990] transition as for the later one. The most similar members to observations in the three models agree with this tendency although they

show weaker variations when compared to observations. The forced signal is, as for precipitation extremes, weak.

To conclude, the three models overestimate changes in the recent recovery shift, not only in total precipitation but also in the contributions linked to the frequency of extreme and heavy rainfall days. In all these contributions, models suggest the recent precipitation recovery is mostly forced and also agree on the dominance of the changes in the frequency of rainfall extremes rather than their intensity in driving Δp. On the contrary, for the [1950-1970] to [1970-1990] transition, models tend to show low relevance of the total externally forced signal, while only some special members show changes consistent in sign and closer in magnitude with the observed precipitation changes, notably in the contributions relating to the change in the frequency of heavy and extreme rainfall days. This highlights the role of internal variability in this early transition.

c. Latitudinal Changes in the Forced Signal of Frequency of Extreme Rainfall Days and Rainy Season Duration

The forced signal consists of longer wet seasons with more cumulative rain and a higher frequency of extreme rainfall days in [1994-2014] driving total Δp (Fig 2). ~~However, this statement does not provide information on how extreme rainfall days are distributed within the rainy season or whether the changes in the frequency of extreme rainfall days and wet season length are homogeneous across all latitudes of the Sahel box. This is what is investigated here.~~ how those changes are distributed in latitude

In order to assess ~~these points~~, Figs. 3a, c and e represent in shading N_e for [1994-2014], [1970-1990] and [1950-1970] respectively. In all cases, extreme rainfall days are most likely to occur in August and September, and are more frequent in the south of the Sahel. In the northernmost tip of the region we barely find days of the year which are at least once an extreme rainfall day after averaging over the Sahel box longitudes. Accordingly, the largest cumulative precipitation occurs in the south of the Sahel, with values of 10 mm d^{-1} between 9°N and 10°N (green contours and white contour for the 10 mm d^{-1} isoline).

The rainy season duration does not vary significantly between the three periods in the south of the Sahel (Fig. 3b), remaining close to 150 days. At the same time, N_e is significantly higher in [1994-2014] (Fig. 3a), than in the other two periods (Figs. 3c and e). Hence, the concentration of extreme rainfall days (r), represented by the three lines in Fig. 3d, is the highest in [1994-2014]

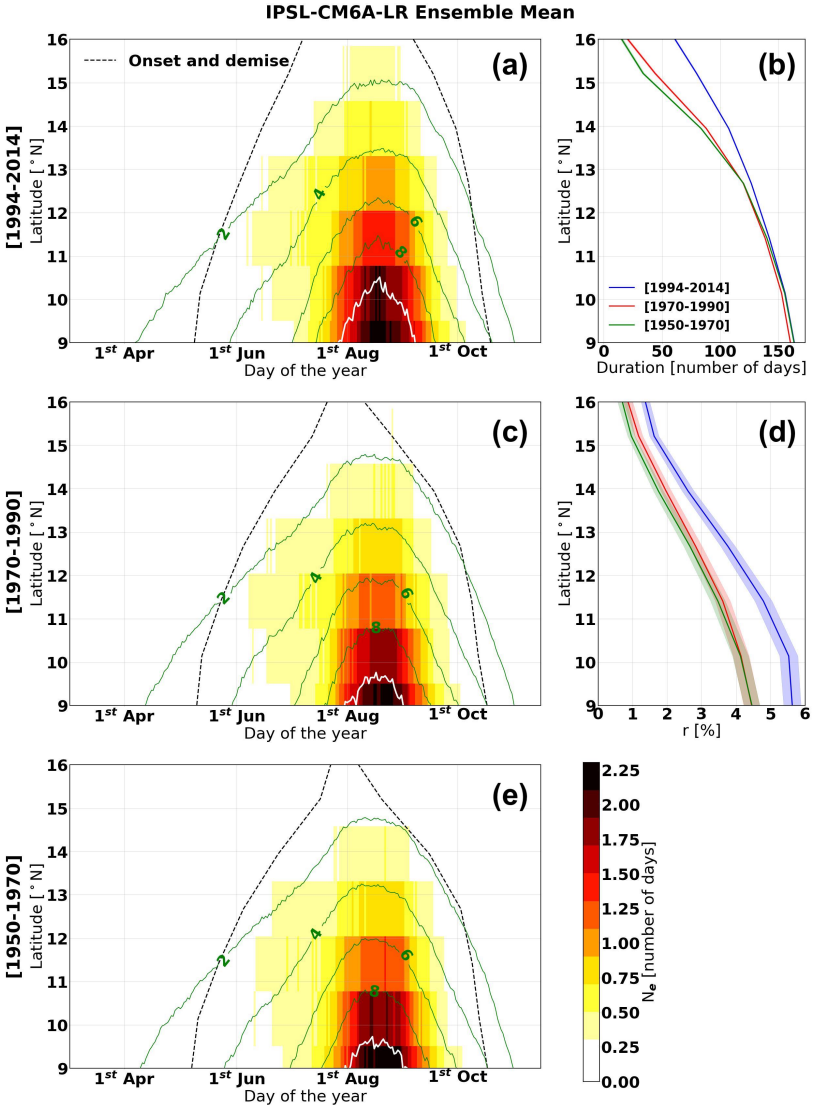

FIG. 3. (a), (c) and (e). The shading represents the number of times a day of the year belongs to the extreme rainfall day category counted for each latitude along all the longitudinal locations of the Sahel box and averaged in the corresponding period of study (N_e, see Section 3). The two dashed lines represent the rainy season onset and demise zonally averaged over the Sahel longitudes, the green contours denote mean precipitation and the white contour represents the 10 mm d^{-1} isoline. These panels represent the periods [1994-2014], [1970-1990] and [1950-1970] respectively. (b) Zonally-averaged rainy season duration in the Sahel box (i.e. difference between the demise and onset dashed lines in panels (a), (c) and (e)) in [1994-2014] (blue), [1970-1990] (red) and [1950-1970] (green). The uncertainty range is omitted since it is much smaller than the rainy season duration values. (d) As in (b) but for the concentration of extreme rainfall days (r, see Section 3), and its associated uncertainty (see Subsection b of the Appendix). This panel uses the same color code as (b). All the results are obtained with the IPSL-CM6A-LR ensemble mean.

(5.5%, blue line) and remains around 4.2% for [1970-1990] and [1950-1970] (red and green curves respectively) in the south of the domain. Note that the uncertainty intervals between [1994-2014] and the other two periods do not overlap (see Subsection b of the Appendix for more details on the error computation procedure). In turn, in the north of the Sahel, the rainy season length increases significantly in [1994-2014] with respect to [1970-1990] and [1950-1970] and so does N_e. However, r is still larger in [1994-2014] (1.5%) than in the other two periods (1% and 0.9% in [1970-1990] and [1950-1970] respectively). Again, the uncertainties in shading do not overlap between [1994-2014] and the other two periods in the north of the Sahel.

These results agree with the ones presented in Figs. 2a and b in terms of the ensemble mean increase in the frequency of extreme rainfall days and rainy season duration in [1994-2014] with respect to [1970-1990]. In addition, they tell us that in recent decades, the south of the Sahel is experiencing more extreme rainfall days concentrated in an equally-long rainy season. On the contrary, the north of the Sahel is experiencing increase in extreme rainfall days which outpaces that of the rainy season length, resulting in a higher concentration of extreme rainfall days too. The similarity between [1950-1970] and [1970-1990] in Fig. 3 highlights again the weak role of the total forced signal in this transition.

We performed the same analysis with CESM2 (Fig. A3) and MIROC6 (Fig. A4). A few differences arise in terms of N_e and rainy season duration: CESM2 and MIROC6 present significantly larger N_e than IPSL-CM6A-LR in the three periods and all latitudes, and MIROC6 shows longer wet seasons in the north of the Sahel than CESM2 and IPSL-CM6A-LR. Yet, the same conclusions for the extreme day concentration of IPSL-CM6A-LR apply to CESM2 and MIROC6.

d. Spatial Pattern of the Multidecadal Variations of Sahel Precipitation Change Contributions

Results from last section only involve the model's ensemble mean (forced signal) and consist of zonal averages in the Sahel box. In this section, we aim to fully assess the spatial pattern of Δp, $\frac{1}{N}\Delta n_e \overline{I_e}$, $\frac{1}{N}\Delta I_e \overline{n_e}$ and $\frac{1}{N}\Delta n_h \overline{I_h}$ of the ensemble mean and the mean of the three most similar members.

Consistently with Fig. 2a, the mean Δp of the IPSL-CM6A-LR three most similar members shows wetter conditions in [1994-2014] than in [1970-1990] which are particularly intense (>0.4 mm d^{-1}) and consistent in the three models (stippling) in central parts of the Sahel (Fig. 4a). The similarity

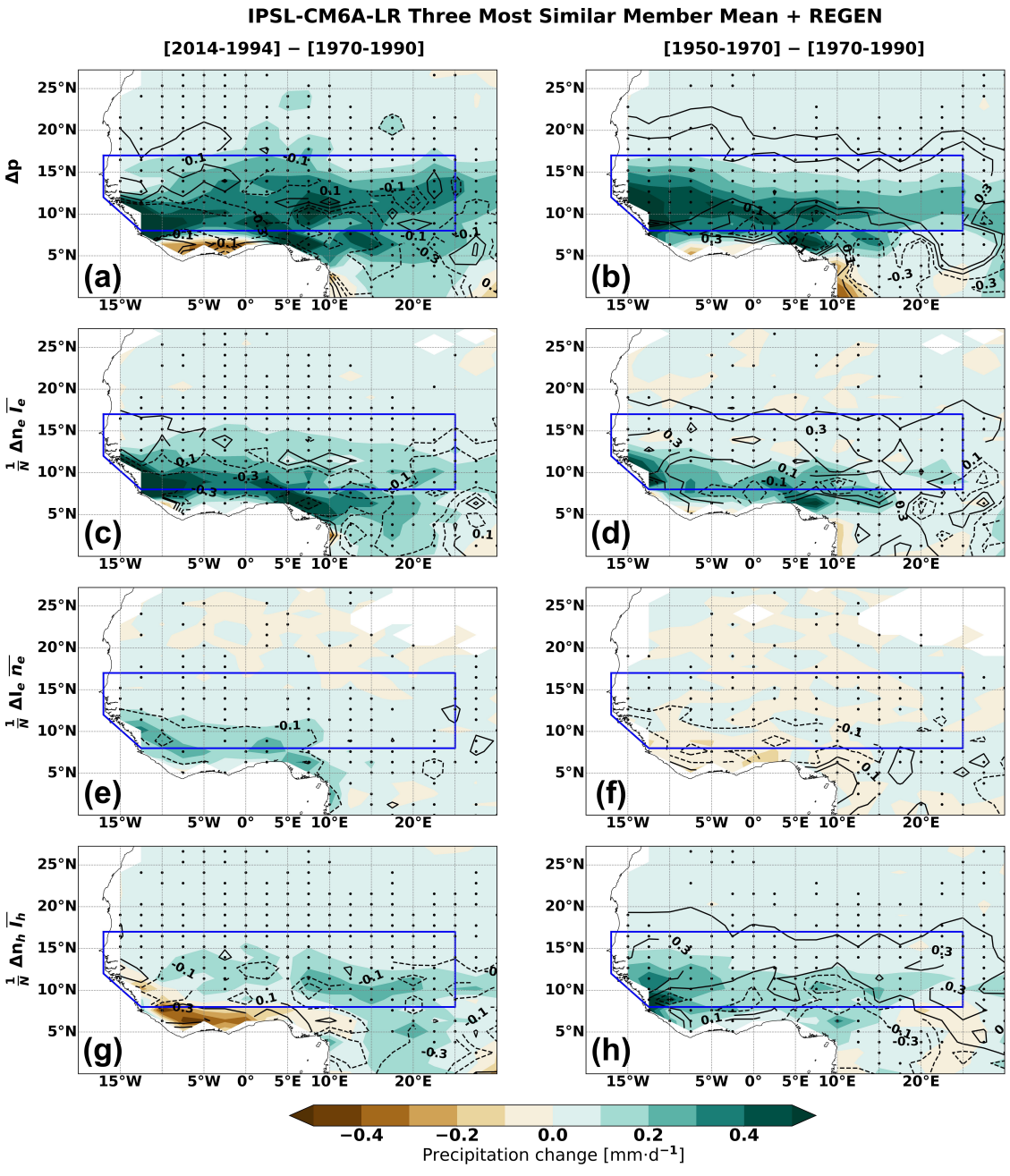

FIG. 4. Spatial pattern of the dominant terms of the precipitation decomposition (Eq. 2) for the mean of the three most similar members of the IPSL-CM6A-LR historical simulation. The stippling indicates locations where the means of the three most similar members of the three model historical simulations (IPSL-CM6A-LR, CESM2 and MIROC6) have the same sign. The solid (dashed) contours represent the differences between REGEN and the mean of the IPSL-CM6A-LR three most similar members when positive (negative). The first column of panels contains the difference between [1994-2014] and [1970-1990] whereas the second column of panels, the change between [1950-1970] and [1970-1990]. In all the panels, the blue box delineates de Sahel. (a) and (b) represent Δp, (c) and (d) $\frac{1}{N}$ Δn$_e$ $\overline{I_e}$, (e) and (f) $\frac{1}{N}$ ΔI$_e$ $\overline{n_e}$ and (g) and (h) $\frac{1}{N}$ Δn$_h$ $\overline{I_h}$.

in the spatial pattern with Fig. 5a which displays the ensemble mean, reveals that this change is mainly forced all over the Sahel box. Note that Δp shows weaker variations in the northeast of the Sahel in both the three most similar member mean and the ensemble mean (Figs. 4a and 5a), in line with the western Sahel drying tendency which appears in future projections (Monerie et al. 2023). Interestingly, this is one of the few regions within the Sahel where the three models underestimate precipitation recovery with respect to REGEN, contrary to the Sahel-averaged overestimation tendency (shown as well in Figs. 1a, A1a and A2a).

Most of the [1970-1990] to [1994-2014] Δp is explained by the contribution associated with the frequency of extreme rainfall days ($\frac{1}{N}\Delta n_e \overline{I_e}$), notably in the south of the Sahel (Fig. 4c). This spatial pattern is consistent in the three models and agrees well with the forced signal tendency (Fig. 4b). Furthermore, the underestimation of the total Δp in this transition with respect to REGEN in the northwest of the Sahel is driven by this term. Finally, Figs. 4e and g display the precipitation contributions tied to the changes in extreme rainfall day intensity and frequency of heavy rainfall days. They act mainly in southwestern and southeastern Sahel respectively, are strongly affected by the forced signal (Figs. 5e and g) and are overestimated in the models with respect to REGEN.

The spatial pattern of the dominant terms in Eq. 2 between [1950-1970] and [1970-1990] is shown in the right column of Fig. 4. Δp (Fig. 4b) is positive, especially in the western part of the Sahel and all three models agree on the sign of the change. This change is, however, weaker than REGEN's throughout the Sahel and it is mostly driven by internal variability. The forced signal (Fig. 5b) only contributes slightly to this change in the western part of the Sahel, where we find Δp increase in the three models.

The mean of the three most similar members' Δp in [1950-1970] to [1970-1990] is driven by both $\frac{1}{N}\Delta n_e \overline{I_e}$ and $\frac{1}{N}\Delta n_h \ \overline{I_h}$ (Figs. 4e and h and in line with Fig. 2a) which act on the south and especially the southwest of the Sahel. Contrary to the [1970-1990] to [1994-2014] transition, the intensity of the extreme events has virtually no contribution (Fig. 4f) and the three models do not agree on the sign of the change. Regarding the forced signal, only $\frac{1}{N}\Delta n_h \overline{I_h}$ displays a weak increase in the west of the Sahel (Fig. 5f) which drives the total Δp forced signal in Fig. 5b.

To conclude, the IPSL-CM6A-LR results represented in Figs. 4 and 5 show that the recent recovery is characterized by a higher frequency of extreme rainfall days which also become more intense particularly in the south of the Sahel. This is in agreement with the observational work

of Le Barbé et al. (2002) and Panthou et al. (2014). In addition, they show that IPSL-CM6A-LR understimates the wetting in the northwestern Sahel with respect to REGEN. This tendency to a weaker wetting in this area agrees with Sow et al. (2025)'s results and becomes more pronounced in future climate projections (Monerie et al. 2023).

Nevertheless, the same analysis for CESM2 and MIROC6 (Figs. A5, A6, A7 and A8) shows that some of these conclusions are model-dependent. While the three models agree on the dominace of $\frac{1}{N}\Delta n_e \overline{I_e}$ in driving precipitation changes in the recent recovery and of $\frac{1}{N}\Delta n_h \overline{I_h}$ forced signal in driving Δp forced signal in the [1950-1970] to [1970-1990] transition, only IPSL-CM6A-LR displays the $\frac{1}{N}\Delta I_e \overline{n_e}$ increase contribution in the [1970-1990] to [1994-2014] shift. In addition, the $\frac{1}{N}\Delta n_h \overline{I_h}$ forced signal also drives together with $\frac{1}{N}\Delta n_e \overline{I_e}$ the total Δp forced signal in the [1950-1970] to [1970-1990] transition. Finally, the three models underestimate the northwestern Sahel precipitation recovery.

e. Effect of Anthropogenic Aerosols and Greenhouse Gases on the Multidecadal Variations of Sahel Precipitation and Intraseasonal Rainfall Features

Up to this point, we have discussed the total forced signal of precipitation and the different terms in Eq. 2. In this section, we aim to assess the impacts of the individual forcings (i.e. GHG and AAs) to the total forced signal. We also tested the contributions of natural external forcings, such as solar and volcanic forcings. They do not significantly modify the results, and we do not consider them here.

Figure 6 shows the Sahel mean forced signal from the IPSL-CM6A-LR historical, hist-aer and hist-GHG simulations. In the [1994-2014] minus [1970-1990] recovery period, the first four bars in Fig. 6a show that 0.10 mm d^{-1} out of the 0.27 mm d^{-1} IPSL-CM6A-LR historical change are associated with AAs and 0.05 mm d^{-1} with GHG. The sum of these two contributions (third bar) is smaller than Δp in the IPSL-CM6A-LR historical mean (fourth bar) although the error bars from both quantities overlap. As a consequence, the hypothesis of linear additivity between AA and GHG cannot be discarded. Similar results were obtained by Shiogama et al. (2023) using MIROC6, also participating in the DAMIP experiment (see their Figs. 3b and d).

The extreme rainfall day contribution in the [1970-1990] to [1994-2014] recovery is shown in the second bar quartet in red in Fig. 6a. Both AAs and GHG contribute equally with an increase of

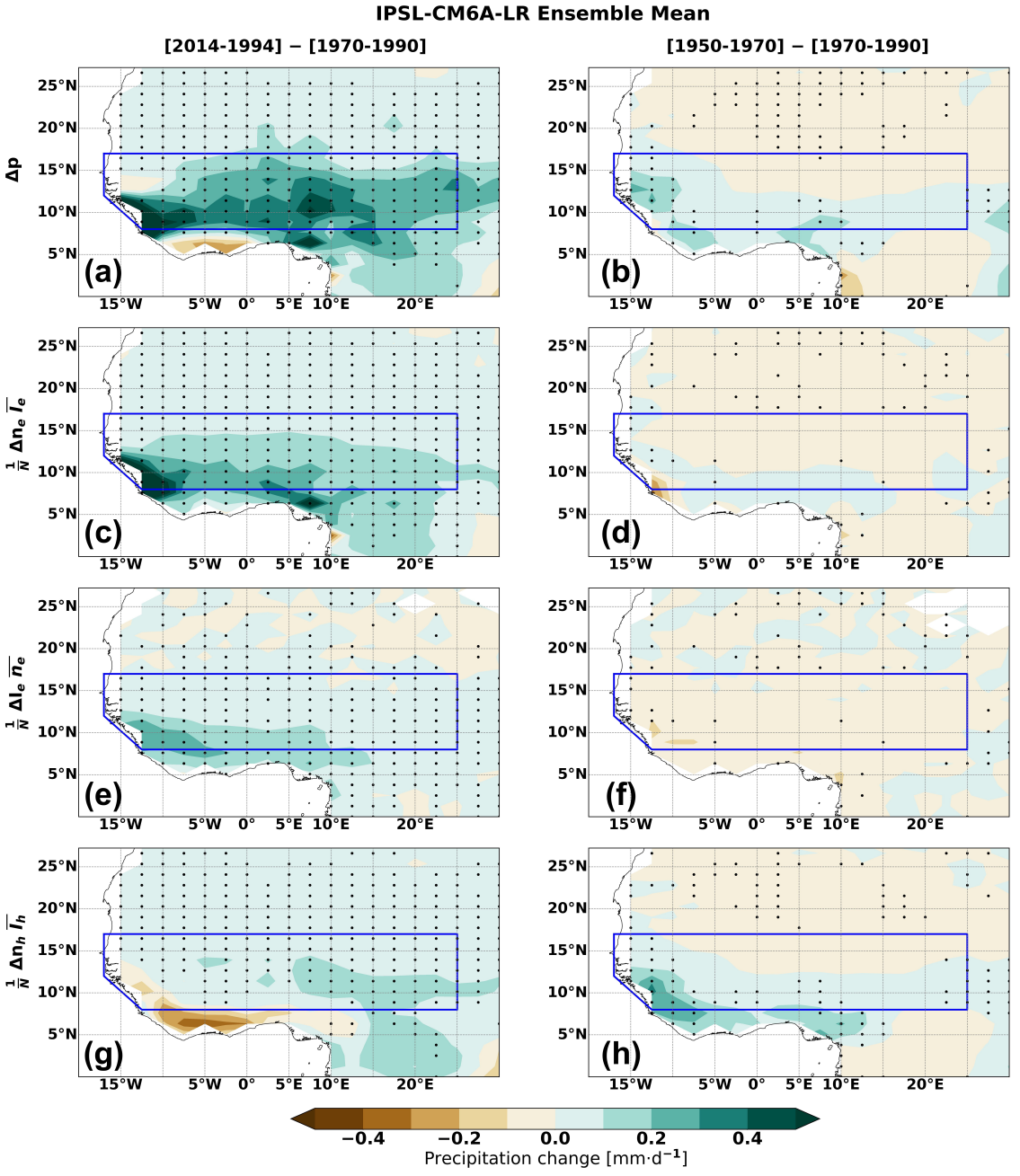

FIG. 5. Spatial pattern of the dominant terms of the precipitation decomposition (Eq. 2) of the IPSL-CM6A-LR historical simulation ensemble mean. The stippling indicates locations where the ensemble means of the three model historical simulations (IPSL-CM6A-LR, CESM2 and MIROC6) have the same sign.The first column of panels contains the difference between [1994-2014] and [1970-1990] whereas the second column of panels, the change between [1950-1970] and [1970-1990]. In all the panels, the blue box delineates de Sahel. (a) and (b) represent Δp, (c) and (d) $\frac{1}{N}$ Δn$_e$ $\overline{I_e}$, (e) and (f) $\frac{1}{N}$ ΔI$_e$ $\overline{n_e}$ and (g) and (h) $\frac{1}{N}$ Δn$_h$ $\overline{I_h}$.

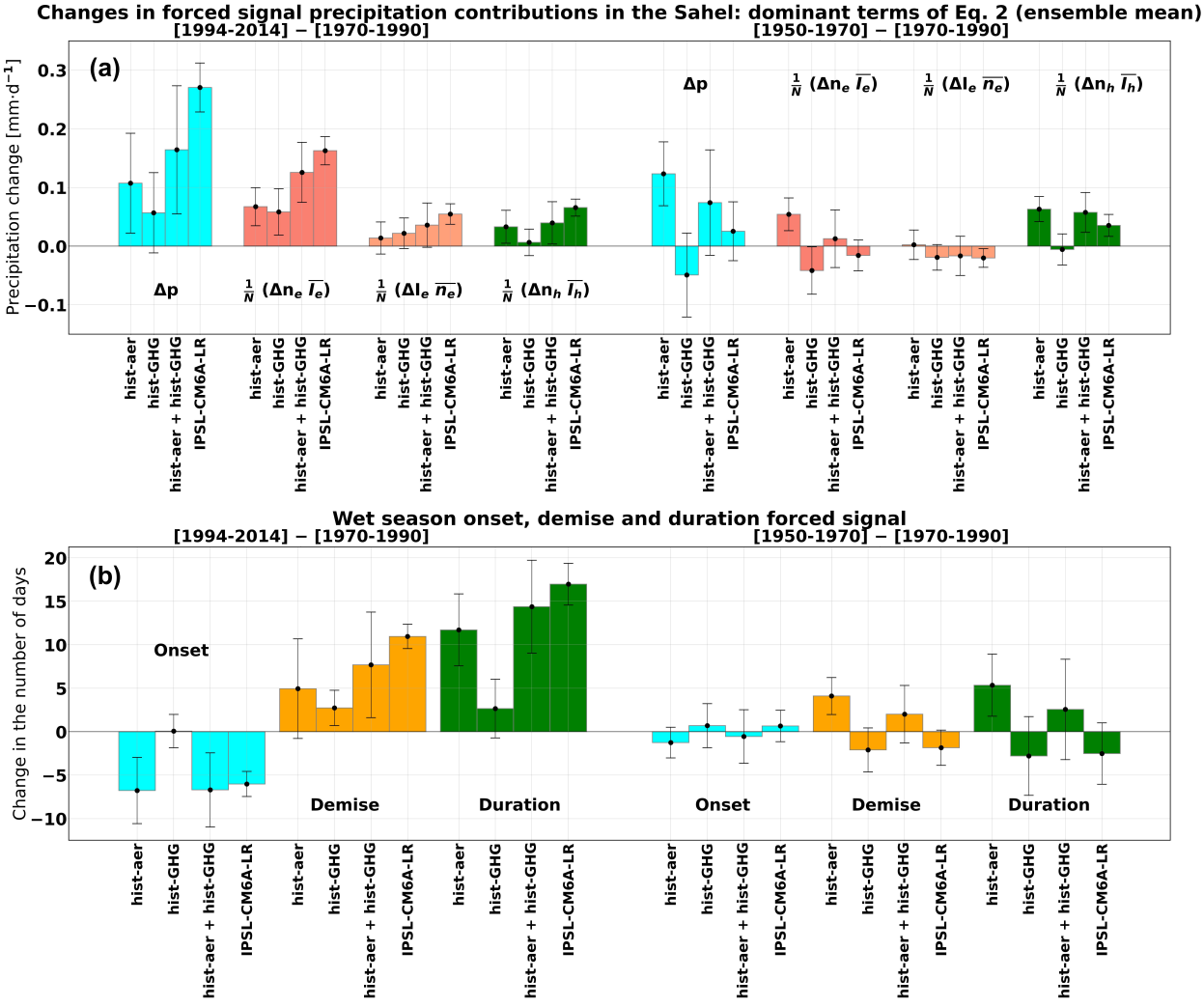

FIG. 6. (a) Bars: Sahel area-weighted mean ensemble mean (forced signal) of the dominant terms from Eq. 2: Δp (cyan), $\frac{1}{N}$ Δn$_e\overline{I_e}$ (red), $\frac{1}{N}$ Δ I$_e\overline{n_e}$ (salmon) and $\frac{1}{N}$ Δ n$_h\overline{I_h}$ (green). The results from [1994-2014] minus [1970-1990] are shown in the four bar quartets on the left and the four bar quartets on the right display [1950-1970] minus [1970-1990]. (b) Same as in (a) but for the wet season onset (cyan), demise (orange) and duration (green). Each bar quartet from both panels, represents, from left to right, the hist-aer, hist-GHG, hist-aer + hist-GHG and IPSL-CM6A-LR historical simulation ensemble means. Error bars display the 95% confidence interval obtained with a two-sided t-test performed along the members of each simulation (24 in hist-aer, 13 in hist-GHG and 32 in the IPSL-CM6A-LR historical simulation). The error interval in hist-aer + hist-GHG is computed applying the error propagation formula.

0.06 mm d^{-1} and 0.05 mm d^{-1} respectively (statistically indistinguishable from zero) being the sum of them (0.13 mm d^{-1}). Its error interval overlaps that of the IPSL-CM6A-LR historical simulation result (linear additivity holds). Note that the expected temperature and moisture increases related to a reduction (increase) of European and North American AAs (GHGs) between [1970-1990] and [1994-2014] close to the surface might act to destabilize the atmosphere above the Sahel and provide more favorable conditions to deep convection and thus a higher frequency of extreme rainfall days (Diakhaté et al. 2019).

The contribution of AAs and GHGs to the extreme rainfall event intensity is smaller, below 0.05 mm d^{-1} in both cases (third bar quartet in salmon in Fig. 6a) and their error intervals include negative values. Finally, the decrease in aerosol concentration between [1970-1990] and [1994-2014] enhances the precipitation change contribution associated with heavy rainfall days. This is not the case for GHG changes, where the error bar covers positive and negative values. Again, the added effect of AA and GHG changes matches the total change in $\frac{1}{N}\Delta n_h \overline{I_h}$ in the limit of the error bars.

In the [1950-1970] to [1970-1990] transition, the Δp forced signal is smaller than in Fig. 2a. However, a different picture emerges from the contributions of the individual forcings. The increase in AA emissions from [1950-1970] to [1970-1990] translates into an decrease in Δp of 0.13 mm d^{-1} (comparable to the results of Monerie et al. 2022), almost equally partitioned between $\frac{1}{N}\Delta n_e \overline{I_e}$ and $\frac{1}{N}\ \Delta n_h\ \overline{I_h}$. In turn, AAs produce little effect over $\frac{1}{N}\Delta I_e \overline{n_e}$, whose error interval covers positive and negative values. GHGs yield an opposite effect in all precipitation contributions and virtually no effect in the precipitation contribution linked to the frequency of heavy rainfall days. This partial compensation between AA and GHG in Δp has already been documented in Monerie et al. (2022) and agrees with the weak total forced signal during this transition documented in previous sections. Furthermore, the dominance of AA over GHG in IPSL-CM6A-LR in setting the decadal modulations of total accumulated Sahel rainfall is in line with Ndiaye et al. (2022) and other studies dealing with specific periods of the twentieth century (Hirasawa et al. 2020). This is yet the first time these changes are systematically assessed in terms of intraseasonal contributions to total precipitation changes.

The changes in the onset, demise and duration of the rainy season associated with each particular forcing are presented in Fig. 6b. The decrease of anthropogenic aerosol concentrations in the

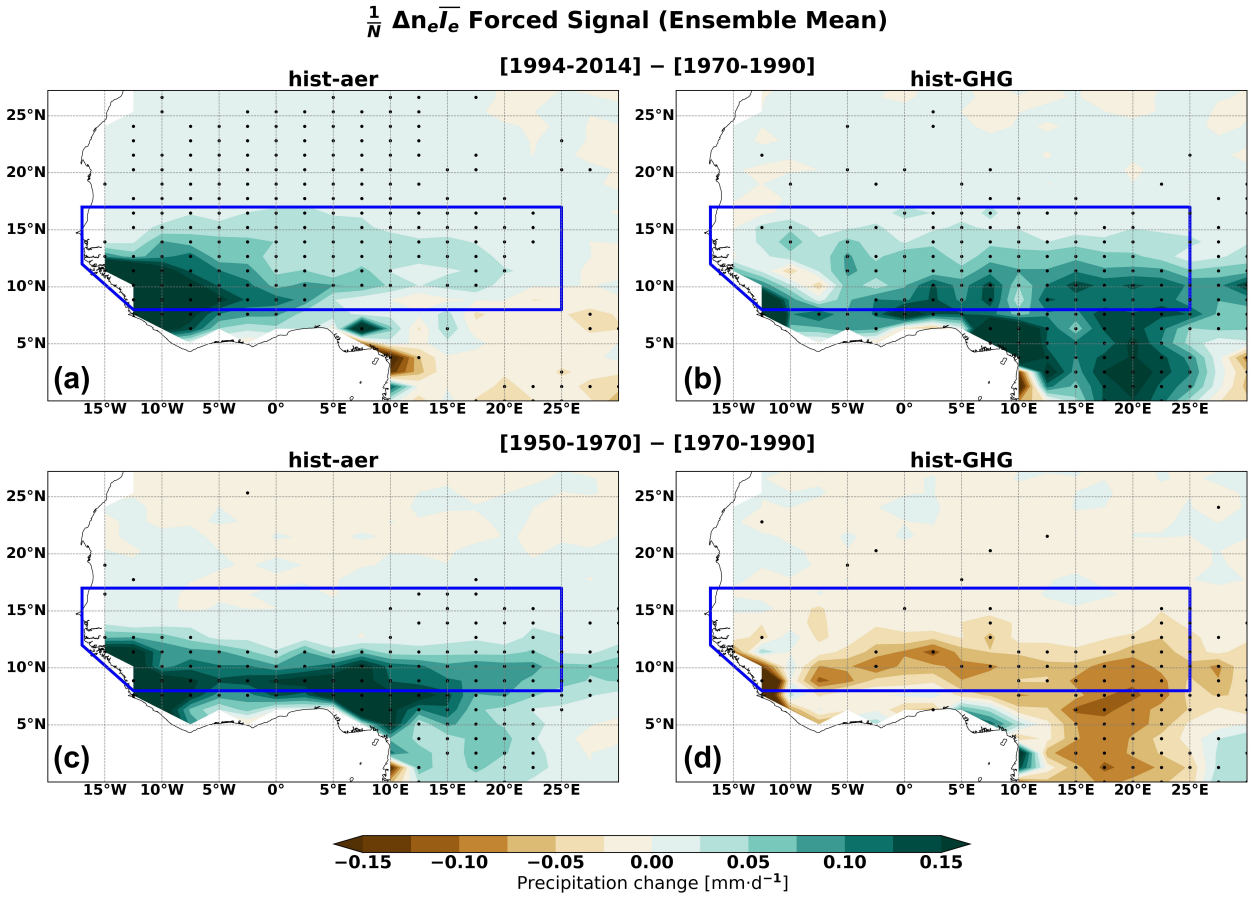

596 FIG. 7. Difference $\frac{1}{N}\,\Delta n_e \overline{I_e}$ between periods for (a) hist-aer [1994-2014] minus [1970-1990], (b) hist-GHG
597 [1994-2014] minus [1970-1990], (c) hist-aer [1950-1970] minus [1970-1990] and (d) hist-GHG [1950-1970]
598 minus [1970-1990]. Stippling covers regions where the differences are statistically significant ($p<0.05$) after a
599 two-sided *t*-test. In all the panels, the blue box delineates the Sahel.

602 [1970-1990] to [1994-2014] transition results in an earlier onset (~-6 d), later demise (~+5 d) and
603 thus a larger monsoon duration of ~11 d. Therefore, reducing the concentration of atmospheric
604 aerosols results in longer rainy seasons. The changes are weaker in the [1950-1970] to [1970-1990]
605 transition, although they go in the same direction. Note that a reduction of AA emissions in North
606 America and Europe reduces SST in the North Atlantic and might result in an earlier northward
607 migration of the ITCZ (Donohoe et al. 2014) thus providing an earlier onset.

608 In turn, GHGs (second bar) do not contribute to change the onset date but help to delay the demise
609 date so that the duration of the season increases under increasing GHG concentrations as well. The

sum hist-aer+hist-GHG of the onset, demise and duration changes is consistent (within error) with the variations obtained directly from the IPSL-CM6A-LR climate simulation in the [1970-1990] to [1994-2014] recovery, supporting the additivity hypothesis among forcing terms. The consistency in the delayed demise response in this transition among all simulations could be related to the increased soil moisture that follows and enhanced rainfall season, since much of the rainfall falling over the Sahel comes from local recycling (Nieto et al. 2006). Finally, in the [1950-1970] to [1970-1990] transition, the sum of hist-aer and hist-GHG presents the opposite tendency to the one obtained with the historical simulation for the onset, demise and duration although the error bars overlap in all cases. An in-depth analysis of the other forcings and the interactions between them is required to elucidate whether there is an important missing contribution here or not.

In order to provide a picture of the spatial distribution of the forcing pattern, Fig. 7 shows the ensemble mean signal of $\frac{1}{N}\Delta n_e \overline{I_e}$ for hist-aer and hist-GHG in both transitions. We choose this term of Eq. 2 since it accounts for most of the variation of the total forced signal in the [1970-1990] to [1994-2014] transition (Fig. 2a) and the three models assessed here display similar forced signal spatial patterns of it (Figs. 5c and d, A7c and d, A8c and d). It shows that while the atmospheric aerosol signal tends to be stronger and more statistically significant in the southwest of the Sahel (Figs. 7a and c), GHGs act primarily in central and eastern parts (Figs. 7b and d), in agreement with Chagnaud et al. (2023). In this respect, Wane et al. (2025) argued that in the context of a warming climate, the global tropics warm faster than a subtropical North Atlantic that is unable to provide sufficient moisture to meet the higher threshold for convection in the adjacent West Sahel (Giannini et al. 2013).

5. Summary and Discussion

In this study, we assess the multidecadal changes of Sahel total rainfall and intraseasonal rainfall features. These are precipitation extreme events in terms of frequency of days and intensity as well as the metrics quantifying the onset, demise and duration of the wet season. To this effect, we make use of observations (REGEN and CRU), large ensembles of historical simulations from three CMIP6 models (IPSL-CM6A-LR, 32 members; CESM2, 84 members and MIROC6, 50 members) and the hist-aer and hist-GHG IPSL-CM6A-LR DAMIP simulations. We focus on

the transitions between the historical humid [1950-1970] and the drier [1970-1990] periods and between [1970-1990] and the recent humid [1994-2014].

Our main findings can be summarized as follows.

- Comparing the IPSL-CM6A-LR historical simulation to its piControl simulation we find that the role of the forced signal in the total Sahel rainfall change is more prominent in the [1970-1990] to [1994-2014] precipitation recovery than in the [1950-1970] to [1970-1990] precipitation reduction. This tendency is also reproduced in CESM2 and MIROC6, and all models agree on an overestimation of the recent recovery and an underestimation of the precipitation decrease between [1950-1970] and [1970-1990] regarding the individual members and the ensemble means.

Be carefull that the aeorsol radiative effect was very small in IPSLCM6ALR. Maybe un derestimated by a factor of 2.

- In the three models, the precipitation change associated with the variation of the frequency of extreme rainfall days is the first order contributor to the total precipitation difference in the [1970-1990] to [1994-2014] precipitation recovery ensemble mean. The same applies to the three most similar members to observations. Note that the variations are not uniform over the Sahel. While the contribution from the frequency of extreme rainfall days is more prominent in the south and southwest, the contribution from the frequency of heavy rainfall days affects mainly central and eastern parts. All three model ensemble means agree on a weaker increase (or even slight decrease) of precipitation during the recovery over Senegal, in line the observational analysis of Badji et al. (2022). In fact, this is the only region in the Sahel where the three models underestimate the precipitation recovery with respect to REGEN. This weaker wetting is shown to then turn into a stronger drying tendency in future climate change projections (Monerie et al. 2023; Wane et al. 2025).

Mal dit.

- The forced signal of the duration of the wet season increases more (in terms of an earlier onset and a later demise) in [1994-2014] than in the other two periods in the north of the Sahel than in the south of the Sahel. At the same time, the forced signal of the frequency of extreme rainfall days increases in all latitudes in [1994-2014]. Both changes result in an increased concentration of extreme rainfall days not only in the south but also in the north of the Sahel since the increase in the frequency of extreme rainfall days outpaces the increase in the wet season duration there. In other words, in recent years the south is experiencing wet season

Concerning the duration of the wet season, there is a forced signal for the [1994-2014] wet period corresponding to an increase, stronger in the north that in the south of the Sahel. There is comparatively almost no signal for the other wet period.

of similar duration than before but with a significantly larger number of extreme rainfall days while in the north wet seasons tend to become longer with more precipitation extremes.

- The contributions of GHGs and AAs in the IPSL-CM6A-LR DAMIP forced signal both contribute to precipitation increase in the [1970-1990] to [1994-2014] transition, notably through changes in the frequency of extreme rainfall days. However, they oppose each other in the [1950-1970] to [1970-1990] transition, in line with the weak total forced signal reported on the historical simulation. For the first time, we show that while AAs mainly affect the number of extreme rainfall days, GHGs impact the contributions linked to both heavy and extreme rainfall days. Finally, the linear additivity of the AA and GHG effects holds in total precipitation and the contributions to total precipitation from the frequency and intensity of extreme rainfall days and the frequency of heavy rainfall days.

This study complements the findings of Sow et al. (2025) by including the multidecadal changes of the different categories of rainy days, and those of Chagnaud et al. (2023) by considering a wider range of intraseasonal rainfall features in Sahel rainfall, notably the linkages between rainy season timing and frequency of extreme rainfall days. In addition, the results presented here are important for agricultural planning over the Sahel. From a user's point of view, even more critical than the total seasonal rainfall is the ability to predict the temporal distribution of rain throughout the season (Salack et al. 2014), which determines the optimal planting and harvesting time (Marteau et al. 2011). In particular, a better understanding of the changes in the recent precipitation recovery is crucial for developing targeted adaptation strategies and allows us to learn more about how intraseasonal rainfall features of Sahel rainfall are likely to evolve in the next decades.

A clear shortcoming of this study is that neither the ensemble mean of coupled historical simulations nor the individual members correctly reproduce the observed precipitation decrease in the [1950-1970] to [1970-1990] transition and the precipitation recovery in the [1970-1990] to [1994-2014] transition. In constrast, we show that the AMIP simulation ensemble (LMDZ, the atmospheric component of IPSL-CM6A-LR forced with observed SSTs) reproduces the precipitation decrease more accurately. This tells us that the coupled historical simulations of the models assessed here do not correctly reproduce either the SST response to forcings and/or its internal variability. Since the effects of external forcings on Sahel rainfall are categorized into two broad pathways (direct atmospheric and ocean mediated, Dong and Sutton 2015; Hirasawa et al. 2020),

future work should seek to understand the drivers of the multidecadal changes in the intraseasonal features of Sahel rainfall with dedicated experiments accounting for these two pathways.

Acknowledgments. The authors acknowledge the funding provided from the *École Université de Recherche* IPSL Climate Graduate School (EUR-IPSL CGR) from which P.F. received funding and the GENCI project, which has been used to extend the DAMIP ensemble. E.M. received funding from the Spanish Ministry of Science and Innovation DISTROPIA project (grant no. PID2021-125806NB-I00). The authors also acknowledge the CESM2 Large Ensemble Community Project and supercomputing resources provided by the IBS Center for Climate Physics in South Korea.

Data availability statement. We benefited from numerous datasets made freely available and listed here.

- The Rainfall Estimate on a Gridded Network all stations version 1 (REGEN) dataset (Contractor et al. 2020): `https://geonetwork.nci.org.au/geonetwork/srv/eng/catalog.search#/metadata/f8555_9260_4736_9502`

- The monthly Climate Research Unit, version 4.01 dataset (CRU TS 4.01, Harris et al. 2020): `https://crudata.uea.ac.uk/cru/data/hrg/`

- The CESM2 large ensemble historical simulation (Rodgers et al. 2021): `https://www.cesm.ucar.edu/community-projects/lens2`

This work was granted access to the HPC resources of SPIRIT and TGCC under the allocation 2025-A0170107403 made by GENCI from where the MIROC6 historical simulation large ensemble and the IPSL-CM6A-LR historical, AMIP and DAMIP simulations were obtained. Due to confidentiality agreements, supporting data can only be made available to bona fide researchers subject to a non-disclosure agreement. Details of the data and how to request access are available from guillaume.gastineau@locean.ipsl.fr at the Laboratoire d'Océanographie et du Climat: Expérimentations et Approches Numériques, Institut Pierre-Simon Laplace, Sorbonne Université/CNRS/IRD/MNHN, Paris, France.

APPENDIX

Supplementary Material

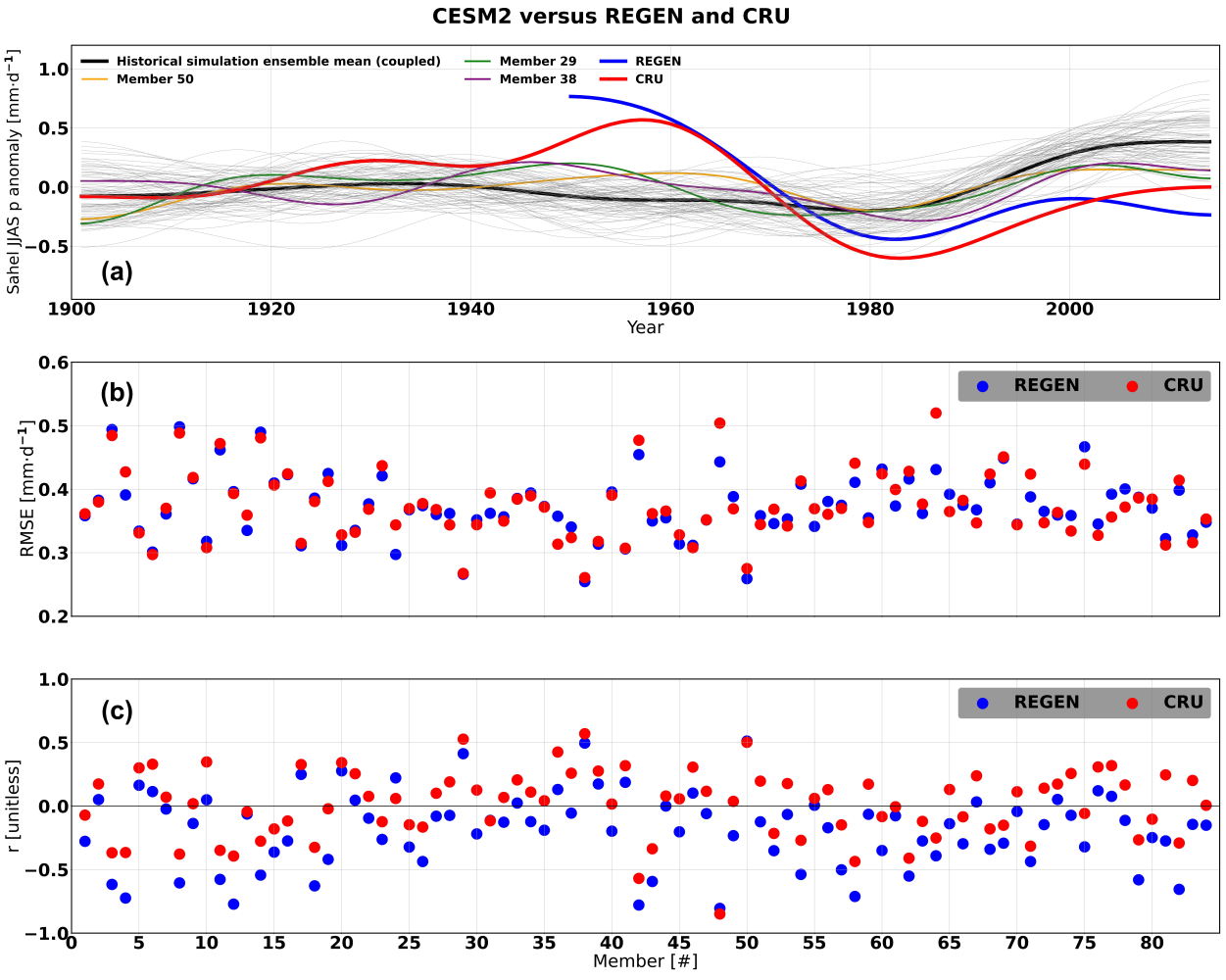

FIG. A1. Like in Fig. 1 but for CESM2

a. Results for CESM2 and MIROC6

b. Error Computation Procedure

In this section we detail the methodology to compute the uncertainties in Table **??**. Given the ensemble mean of the mean value in a period of study of a variable (X), we can estimate its uncertainty (ΔX) as:

$$\Delta X = \sqrt{\left(\frac{s_{\text{year}}}{\sqrt{n_{\text{year}}}}\right)^2 + \left(\frac{s_{\text{member}}}{\sqrt{n_{\text{member}}}}\right)^2} \tag{A1}$$

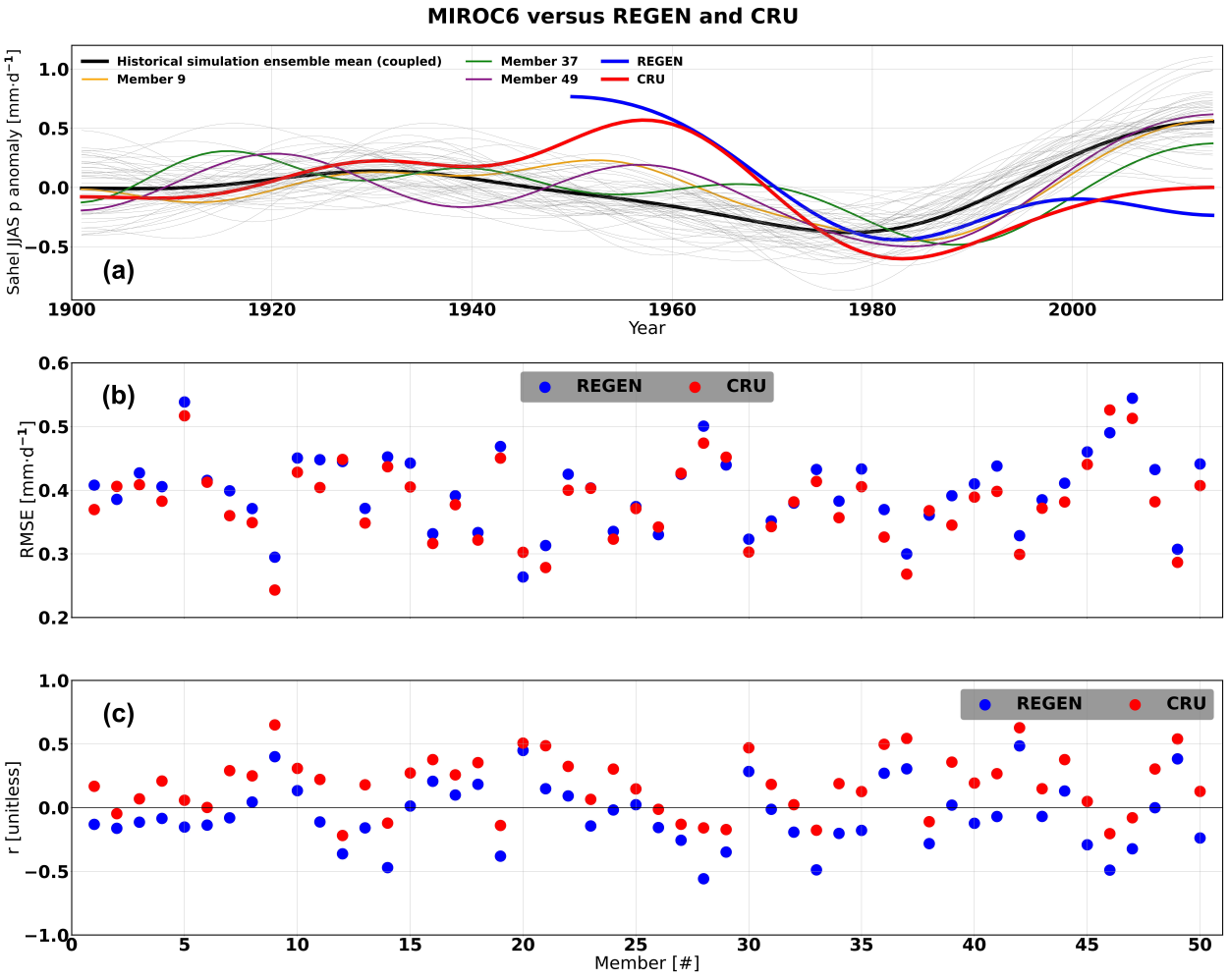

FIG. A2. Like in Fig. 1 and A1 but for MIROC6

where n_{year} and n_{member} are the number of years in a period (i.e. 21) and the number of members of the ensemble respectively. s_{year} and s_{member} denote, respectively, the standard deviations computed along the time and member dimensions.

Therefore, given ΔN_e and ΔL, the uncertainties in the number of times a day of the year is a extreme rainfall days in a specific latitude and the rainy season duration estimated with Eq. A2, applying the error propagation formula to Eq. 3 we obtain:

$$\Delta r = r \sqrt{\left(\frac{\Delta N_e}{N_e}\right)^2 + \left(\frac{\Delta L}{L}\right)^2} \tag{A2}$$

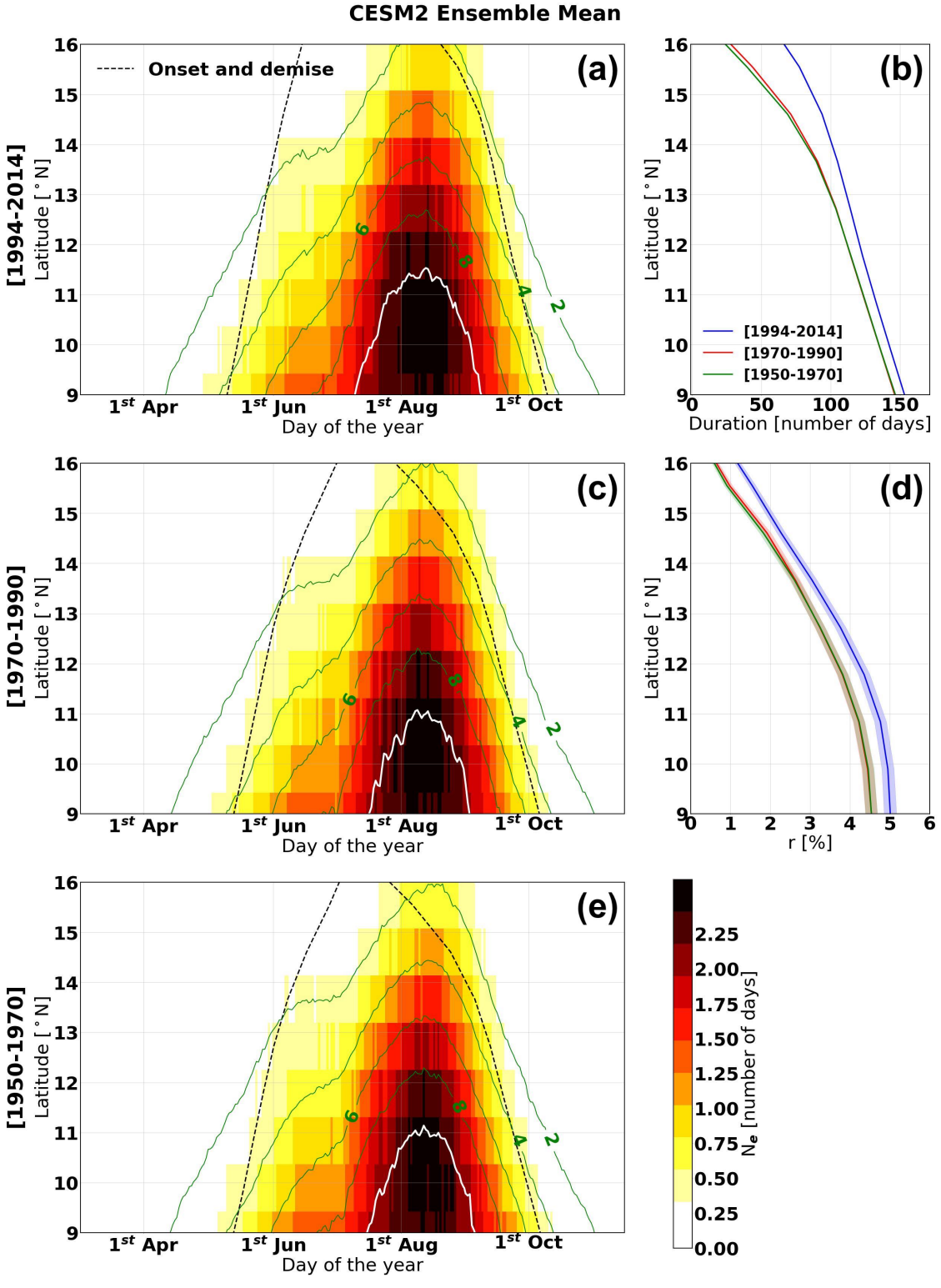

FIG. A3. Like in Fig. 3 but for CESM2

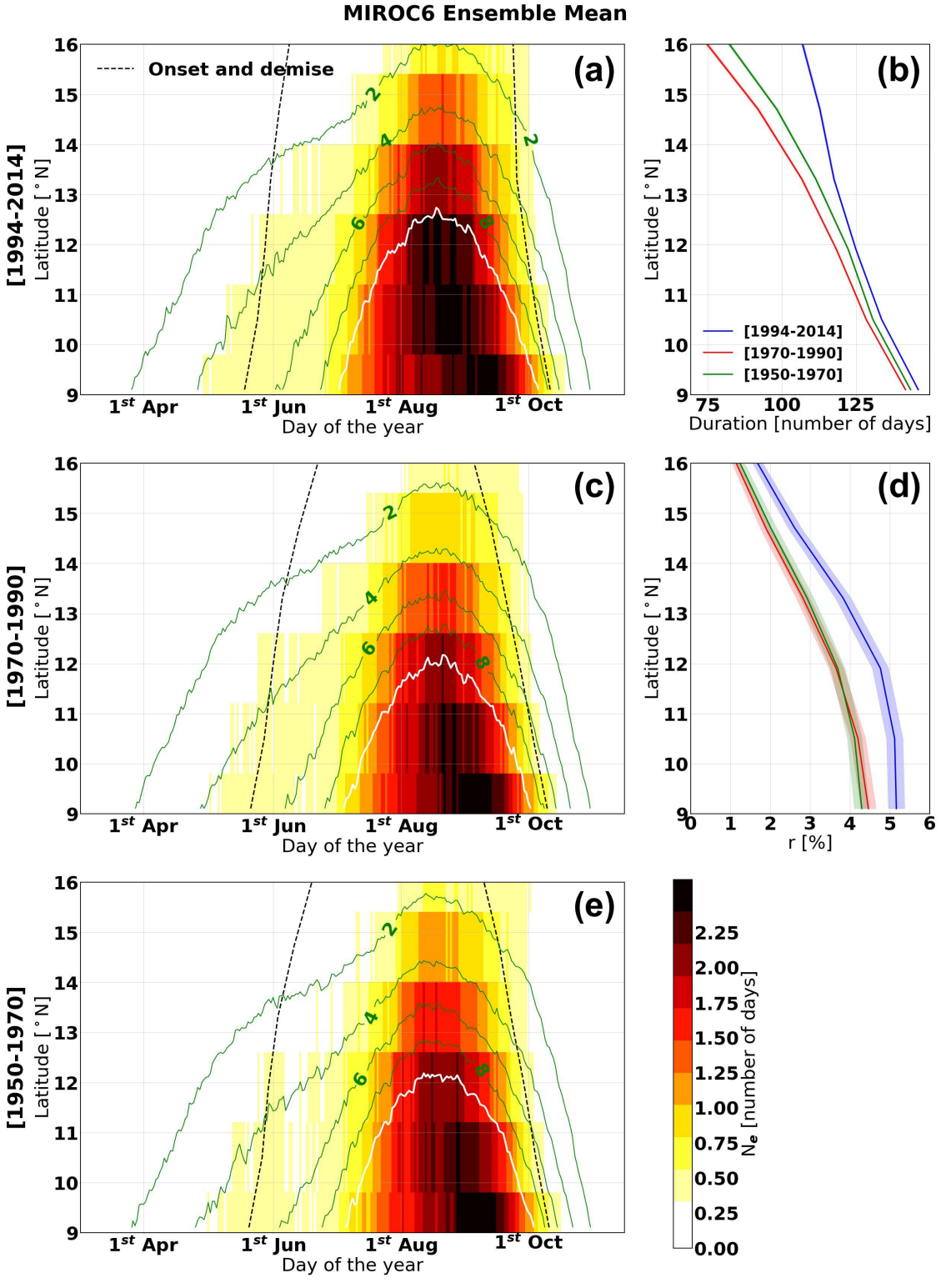

FIG. A4. Like in Fig. 3 and A3 but for MIROC6

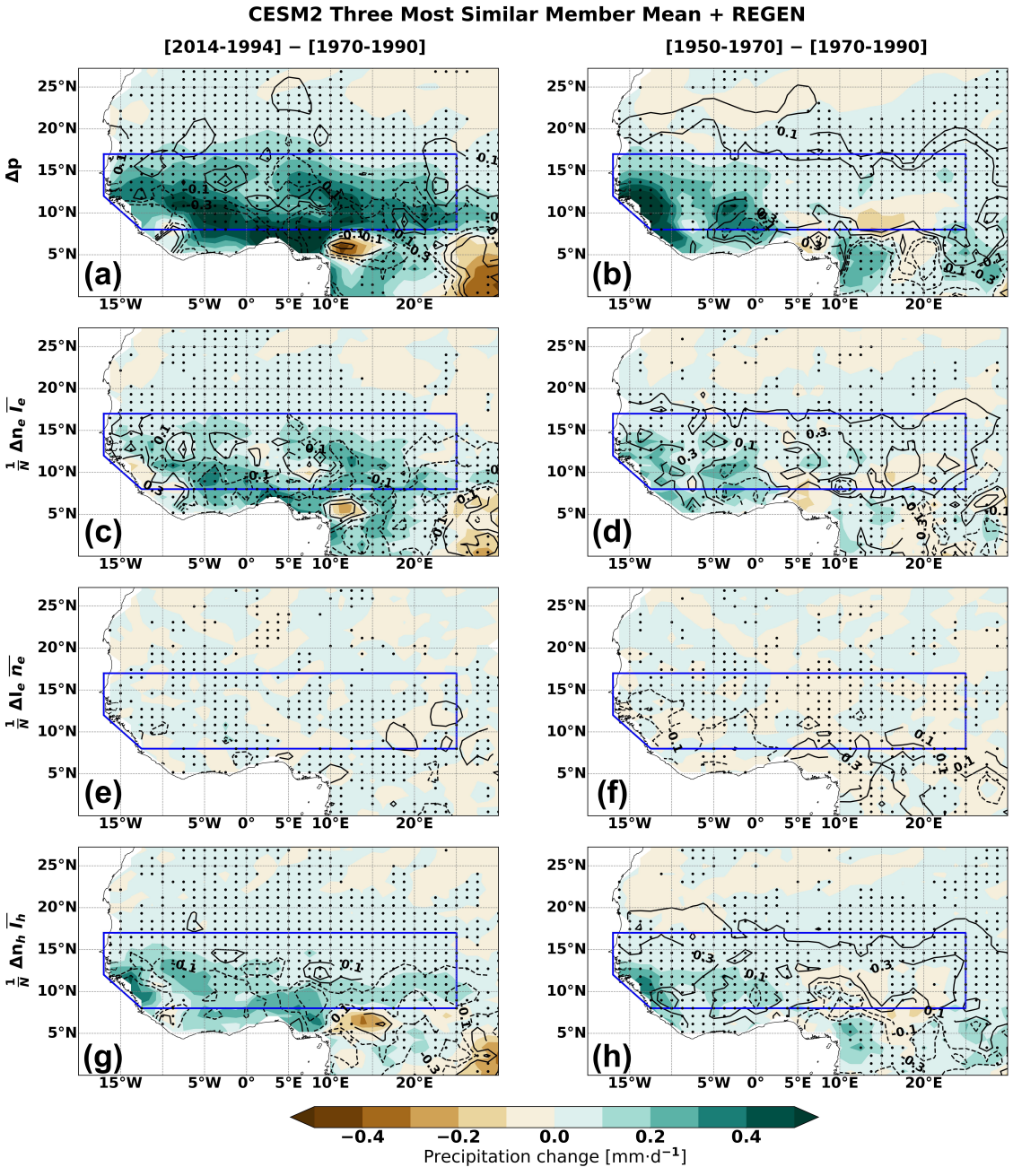

FIG. A5. Like in Fig. 4 but for CESM2

References

Ackerley, D., B. B. Booth, S. H. Knight, E. J. Highwood, D. J. Frame, M. R. Allen, and D. P. Rowell, 2011: Sensitivity of twentieth-century sahel rainfall to sulfate aerosol and co 2 forcing. *Journal of Climate*, **24 (19)**, 4999–5014.

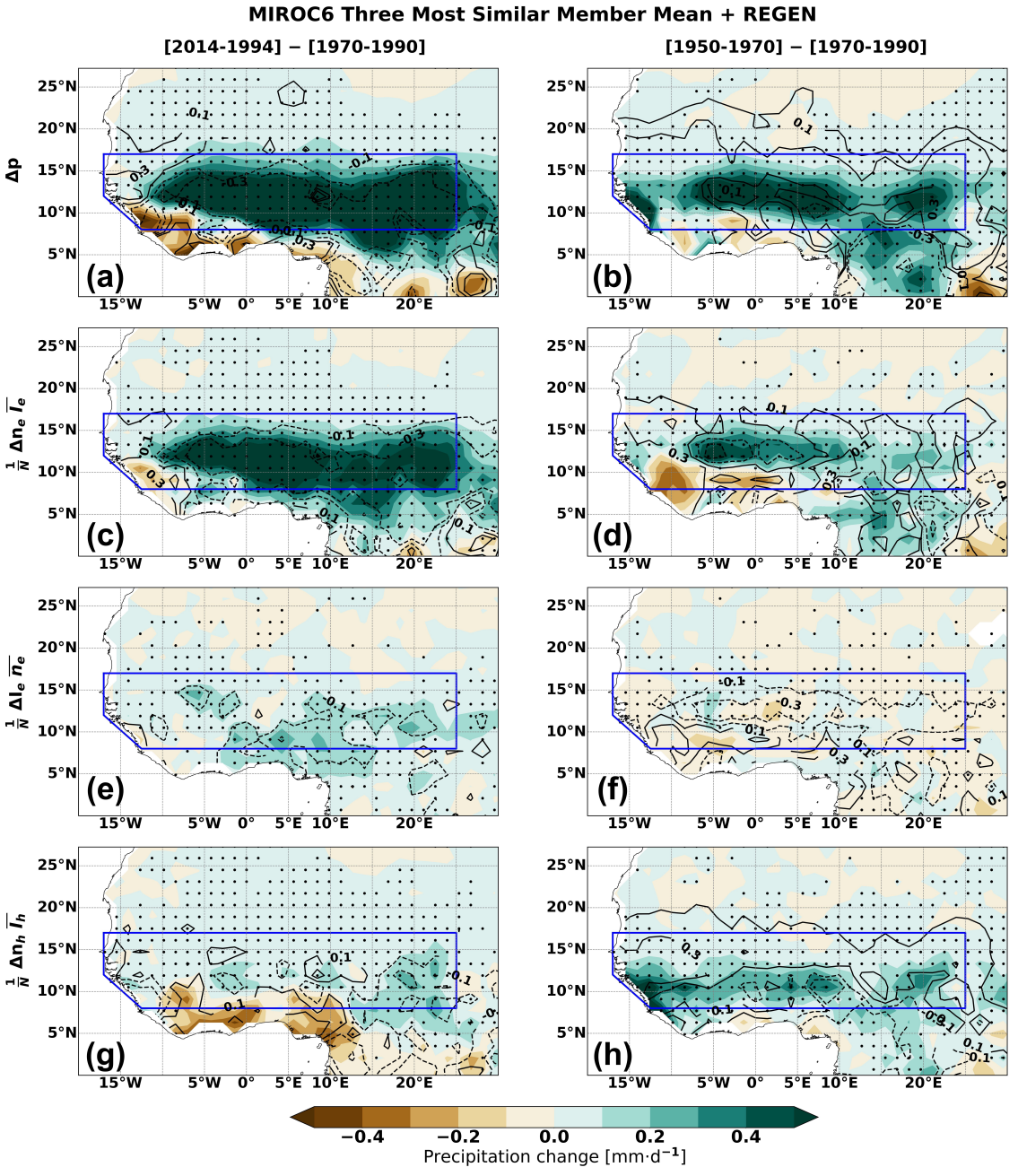

FIG. A6. Like in Fig. 4 and A5 but for MIROC6

Badji, A., E. Mohino, M. Diakhaté, J. Mignot, and A. T. Gaye, 2022: Decadal variability of rainfall in senegal: Beyond the total seasonal amount. *Journal of Climate*, **35 (16)**, 5339–5358.

Bellomo, K., L. N. Murphy, M. A. Cane, A. C. Clement, and L. M. Polvani, 2018: Historical forcings as main drivers of the atlantic multidecadal variability in the cesm large ensemble.

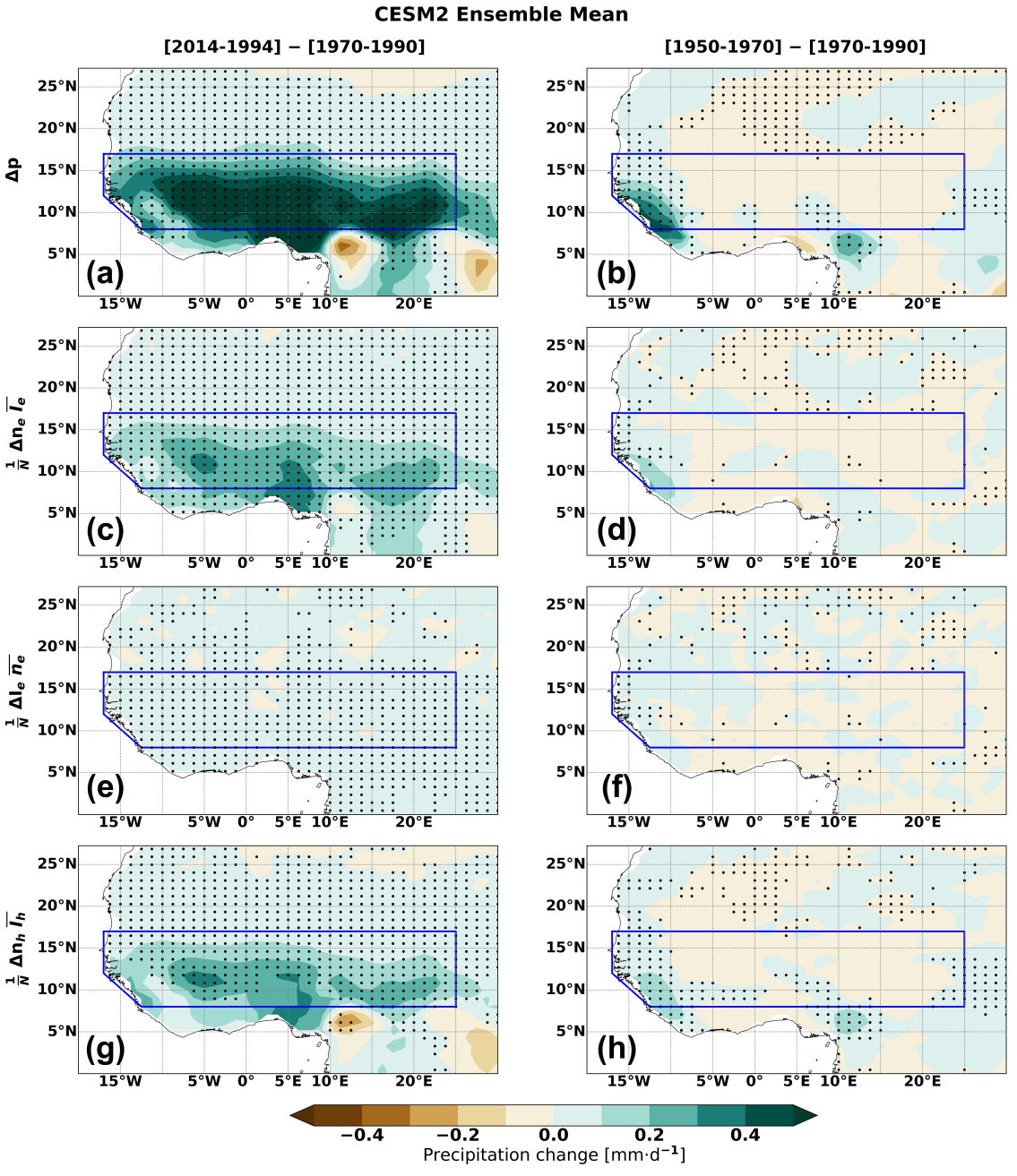

FIG. A7. Like in Fig. 5 but for CESM2

Climate dynamics, **50 (9)**, 3687–3698.

Berntell, E., Q. Zhang, L. Chafik, and H. Körnich, 2018: Representation of multidecadal sahel rainfall variability in 20th century reanalyses. *Scientific reports*, **8 (1)**, 10 937.

Biasutti, M., 2011: A man-made drought. *Nature Climate Change*, **1 (4)**, 197–198.

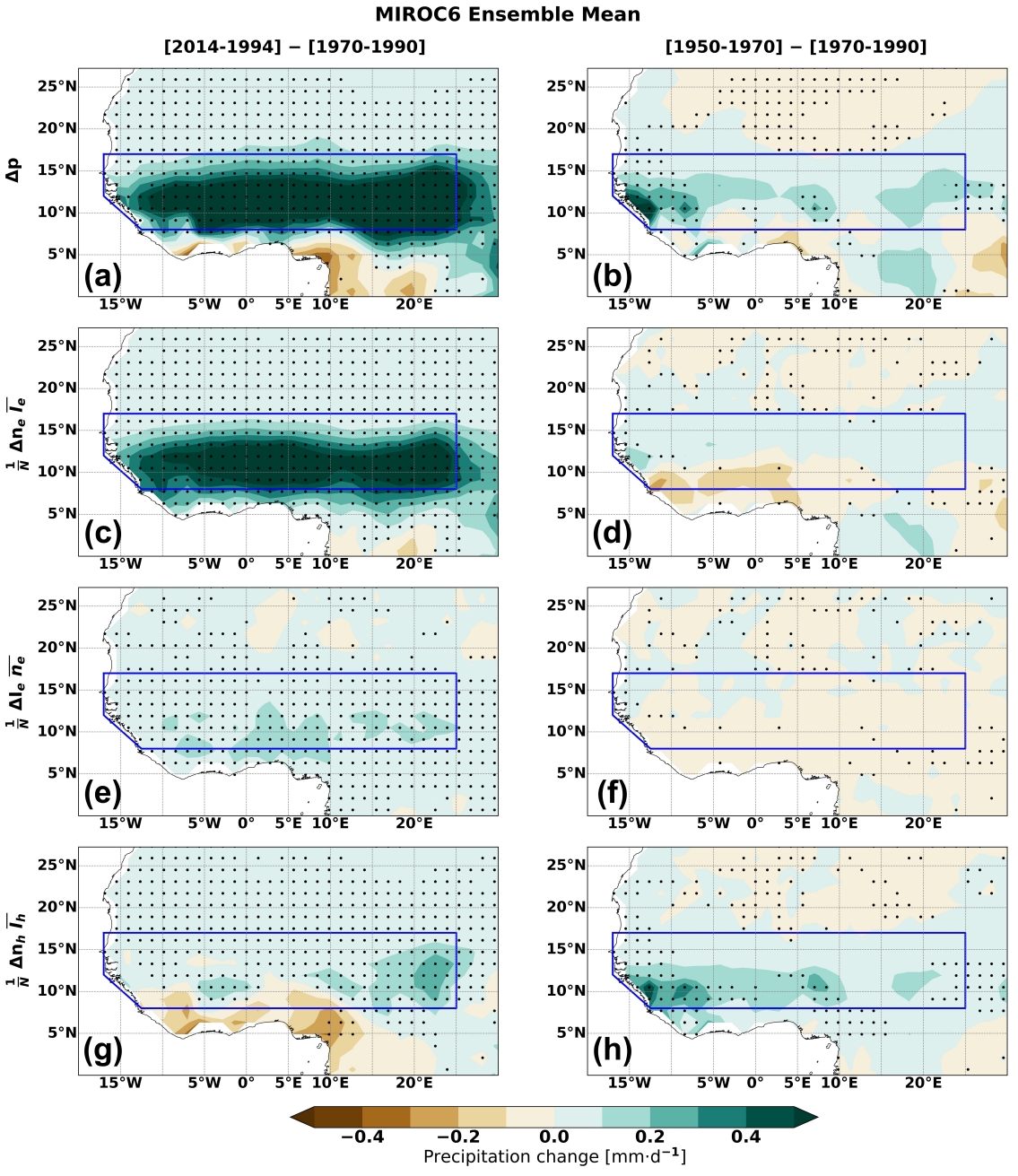

FIG. A8. Like in Fig. 5 and A7 but for MIROC6

747 Biasutti, M., 2019: Rainfall trends in the african sahel: Characteristics, processes, and causes.
748 *Wiley Interdisciplinary Reviews: Climate Change*, **10 (4)**, e591.

749 Biasutti, M., and A. Giannini, 2006: Robust sahel drying in response to late 20th century forcings.
750 *Geophysical Research Letters*, **33 (11)**.

Blanchet, J., C. Aly, T. Vischel, G. Panthou, Y. Sané, and M. Diop Kane, 2018: Trend in the co-occurrence of extreme daily rainfall in west africa since 1950. *Journal of Geophysical Research: Atmospheres*, **123 (3)**, 1536–1551.

Bonnet, R., O. Boucher, J. Deshayes, G. Gastineau, F. Hourdin, J. Mignot, J. Servonnat, and D. Swingedouw, 2021a: Presentation and evaluation of the ipsl-cm6a-lr ensemble of extended historical simulations. *Journal of Advances in Modeling Earth Systems*, **13 (9)**, e2021MS002 565.

Bonnet, R., and Coauthors, 2021b: Increased risk of near term global warming due to a recent amoc weakening. *Nature communications*, **12 (1)**, 6108.

Booth, B. B., N. J. Dunstone, P. R. Halloran, T. Andrews, and N. Bellouin, 2012: Aerosols implicated as a prime driver of twentieth-century north atlantic climate variability. *Nature*, **484 (7393)**, 228–232.

Boucher, O., and Coauthors, 2020: Presentation and evaluation of the ipsl-cm6a-lr climate model. *Journal of Advances in Modeling Earth Systems*, **12 (7)**, e2019MS002 010.

Chagnaud, G., G. Panthou, T. Vischel, and T. Lebel, 2022: A synthetic view of rainfall intensification in the west african sahel. *Environmental Research Letters*, **17 (4)**, 044 005.

Chagnaud, G., G. Panthou, T. Vischel, and T. Lebel, 2023: Capturing and attributing the rainfall regime intensification in the west african sahel with cmip6 models. *Journal of Climate*, **36 (6)**, 1823–1843.

Clement, A., K. Bellomo, L. N. Murphy, M. A. Cane, T. Mauritsen, G. Rädel, and B. Stevens, 2015: The atlantic multidecadal oscillation without a role for ocean circulation. *Science*, **350 (6258)**, 320–324.

Contractor, S., and Coauthors, 2020: Rainfall estimates on a gridded network (regen)–a global land-based gridded dataset of daily precipitation from 1950 to 2016. *Hydrology and Earth System Sciences*, **24 (2)**, 919–943.

Danabasoglu, G., and Coauthors, 2020: The community earth system model version 2 (cesm2). *Journal of Advances in Modeling Earth Systems*, **12 (2)**, e2019MS001 916.

Diakhaté, M., B. Rodriguez-Fonseca, I. Gómara, E. Mohino, A. L. Dieng, and A. T. Gaye, 2019: Oceanic forcing on interannual variability of sahel heavy and moderate daily rainfall. *Journal of Hydrometeorology*, **20 (3)**, 397–410.

Dong, B., and R. Sutton, 2015: Dominant role of greenhouse-gas forcing in the recovery of sahel rainfall. *Nature Climate Change*, **5 (8)**, 757–760.

Donohoe, A., J. Marshall, D. Ferreira, K. Armour, and D. McGee, 2014: The interannual variability of tropical precipitation and interhemispheric energy transport. *Journal of Climate*, **27 (9)**, 3377–3392.

Eyring, V., S. Bony, G. A. Meehl, C. A. Senior, B. Stevens, R. J. Stouffer, and K. E. Taylor, 2016: Overview of the coupled model intercomparison project phase 6 (cmip6) experimental design and organization. *Geoscientific Model Development*, **9 (5)**, 1937–1958.

Folland, C. K., T. N. Palmer, and D. E. Parker, 1986: Sahel rainfall and worldwide sea temperatures, 1901–85. *Nature*, **320 (6063)**, 602–607.

Fyfe, J. C., V. V. Kharin, B. D. Santer, J. N. Cole, and N. P. Gillett, 2021: Significant impact of forcing uncertainty in a large ensemble of climate model simulations. *Proceedings of the National Academy of Sciences*, **118 (23)**, e2016549 118.

Giannini, A., and A. Kaplan, 2019: The role of aerosols and greenhouse gases in sahel drought and recovery. *Climatic Change*, **152 (3)**, 449–466.

Giannini, A., S. Salack, T. Lodoun, A. Ali, A. Gaye, and O. Ndiaye, 2013: A unifying view of climate change in the sahel linking intra-seasonal, interannual and longer time scales. *Environmental Research Letters*, **8 (2)**, 024 010.

Giannini, A., R. Saravanan, and P. Chang, 2003: Oceanic forcing of sahel rainfall on interannual to interdecadal time scales. *Science*, **302 (5647)**, 1027–1030.

Gillett, N. P., and Coauthors, 2016: The detection and attribution model intercomparison project (damip v1. 0) contribution to cmip6. *Geoscientific Model Development*, **9 (10)**, 3685–3697.

Guilbert, M., P. Terray, J. Mignot, L. Ollier, and G. Gastineau, 2024: Interhemispheric temperature gradient and equatorial pacific ssts drive sahel monsoon uncertainties under global warming. *Journal of Climate*, **37 (3)**, 1033–1052.

Harris, I., T. J. Osborn, P. Jones, and D. Lister, 2020: Version 4 of the cru ts monthly high-resolution gridded multivariate climate dataset. *Scientific data*, **7 (1)**, 109.

Hartmann, D. L., and Coauthors, 2013: Observations: atmosphere and surface. *Climate change 2013 the physical science basis: Working group I contribution to the fifth assessment report of the intergovernmental panel on climate change*, Cambridge University Press, 159–254.

Herold, N., L. Alexander, M. Donat, S. Contractor, and A. Becker, 2016: How much does it rain over land? *Geophysical Research Letters*, **43 (1)**, 341–348.

Hirasawa, H., P. J. Kushner, M. Sigmond, J. Fyfe, and C. Deser, 2020: Anthropogenic aerosols dominate forced multidecadal sahel precipitation change through distinct atmospheric and oceanic drivers. *Journal of Climate*, **33 (23)**, 10 187–10 204.

Hirasawa, H., P. J. Kushner, M. Sigmond, J. Fyfe, and C. Deser, 2022: Evolving sahel rainfall response to anthropogenic aerosols driven by shifting regional oceanic and emission influences. *Journal of Climate*, **35 (11)**, 3181–3193.

Kawase, H., M. Abe, Y. Yamada, T. Takemura, T. Yokohata, and T. Nozawa, 2010: Physical mechanism of long-term drying trend over tropical north africa. *Geophysical Research Letters*, **37 (9)**.

Kay, J. E., and Coauthors, 2015: The community earth system model (cesm) large ensemble project: A community resource for studying climate change in the presence of internal climate variability. *Bulletin of the American Meteorological Society*, **96 (8)**, 1333–1349.

Kitoh, A., E. Mohino, Y. Ding, K. Rajendran, T. Ambrizzi, J. Marengo, and V. Magaña, 2020: Combined oceanic influences on continental climates. *Interacting climates of ocean basins: observations, mechanisms, predictability, and impacts. 1ed. New York, USA: Cambridge University Press*, **1**, 216–249.

828 Klavans, J. M., A. C. Clement, M. A. Cane, and L. N. Murphy, 2022: The evolving role of external
829 forcing in north atlantic sst variability over the last millennium. *Journal of Climate*, **35 (9)**,
830 2741–2754.

831 Klutse, N. A. B., K. A. Quagraine, F. Nkrumah, K. T. Quagraine, R. Berkoh-Oforiwaa, J. F. Dzrobi,
832 and M. B. Sylla, 2021: The climatic analysis of summer monsoon extreme precipitation events
833 over west africa in cmip6 simulations. *Earth Systems and Environment*, **5**, 25–41.

834 Knight, J. R., 2009: The atlantic multidecadal oscillation inferred from the forced climate response
835 in coupled general circulation models. *Journal of Climate*, **22 (7)**, 1610–1625.

836 Knight, J. R., R. J. Allan, C. K. Folland, M. Vellinga, and M. E. Mann, 2005: A signature of
837 persistent natural thermohaline circulation cycles in observed climate. *Geophysical Research*
838 *Letters*, **32 (20)**.

839 Le Barbé, L., T. Lebel, and D. Tapsoba, 2002: Rainfall variability in west africa during the years
840 1950–90. *Journal of climate*, **15 (2)**, 187–202.

841 Lebel, T., and A. Ali, 2009: Recent trends in the central and western sahel rainfall regime (1990–
842 2007). *Journal of hydrology*, **375 (1-2)**, 52–64.

843 Liebmann, B., I. Bladé, G. N. Kiladis, L. M. Carvalho, G. B. Senay, D. Allured, S. Leroux, and
844 C. Funk, 2012: Seasonality of african precipitation from 1996 to 2009. *Journal of Climate*,
845 **25 (12)**, 4304–4322.

846 Losada, T., B. Rodríguez-Fonseca, S. Janicot, S. Gervois, F. Chauvin, and P. Ruti, 2010: A multi-
847 model approach to the atlantic equatorial mode: impact on the west african monsoon. *Climate*
848 *Dynamics*, **35**, 29–43.

849 Mann, M. E., B. A. Steinman, D. J. Brouillette, and S. K. Miller, 2021: Multidecadal climate
850 oscillations during the past millennium driven by volcanic forcing. *Science*, **371 (6533)**, 1014–
851 1019.

852 Marteau, R., 2010: Cohérence spatiale et previsibilité potentielle des descripteurs intrasaisonniers
853 de la saison des pluies en afrique soudano-sahélienne: Application à la culture du mil dans la
854 région de niamey. Ph.D. thesis, Université de Bourgogne.

Marteau, R., B. Sultan, V. Moron, A. Alhassane, C. Baron, and S. B. Traoré, 2011: The onset of the rainy season and farmers' sowing strategy for pearl millet cultivation in southwest niger. *Agricultural and forest meteorology*, **151 (10)**, 1356–1369.

Menary, M. B., and Coauthors, 2020: Aerosol-forced amoc changes in cmip6 historical simulations. *Geophysical Research Letters*, **47 (14)**, e2020GL088 166.

Mohino, E., S. Janicot, and J. Bader, 2011: Sahel rainfall and decadal to multi-decadal sea surface temperature variability. *Climate dynamics*, **37**, 419–440.

Mohino, E., P.-A. Monerie, J. Mignot, M. Diakhaté, M. Donat, C. D. Roberts, and F. Doblas-Reyes, 2024: Impact of atlantic multidecadal variability on rainfall intensity distribution and timing of the west african monsoon. *Earth System Dynamics*, **15 (1)**, 15–40.

Monerie, P.-A., M. Biasutti, J. Mignot, E. Mohino, B. Pohl, and G. Zappa, 2023: Storylines of sahel precipitation change: Roles of the north atlantic and euro-mediterranean temperature. *Journal of Geophysical Research: Atmospheres*, **128 (16)**, e2023JD038 712.

Monerie, P.-A., L. J. Wilcox, and A. G. Turner, 2022: Effects of anthropogenic aerosol and greenhouse gas emissions on northern hemisphere monsoon precipitation: Mechanisms and uncertainty. *Journal of Climate*, **35 (8)**, 2305–2326.

Ndiaye, C. D., E. Mohino, J. Mignot, and S. M. Sall, 2022: On the detection of externally forced decadal modulations of the sahel rainfall over the whole twentieth century in the cmip6 ensemble. *Journal of Climate*, **35 (21)**, 6939–6954.

Nicholson, S. E., 1983: Sub-saharan rainfall in the years 1976–80: evidence of continued drought. *Monthly weather review*, **111 (8)**, 1646–1654.

Nicholson, S. E., 2013: The west african sahel: A review of recent studies on the rainfall regime and its interannual variability. *International Scholarly Research Notices*, **2013 (1)**, 453 521.

Nieto, R., L. Gimeno, and R. M. Trigo, 2006: A lagrangian identification of major sources of sahel moisture. *Geophysical Research Letters*, **33 (18)**.

Panthou, G., T. Vischel, and T. Lebel, 2014: Recent trends in the regime of extreme rainfall in the central sahel. *International Journal of Climatology*, **34 (15)**.

Panthou, G., and Coauthors, 2018: Rainfall intensification in tropical semi-arid regions: the sahelian case. *Environmental Research Letters*, **13 (6)**, 064 013.

Rodgers, K. B., and Coauthors, 2021: Ubiquity of human-induced changes in climate variability. *Earth System Dynamics*, **12 (4)**, 1393–1411.

Rodríguez-Fonseca, B., and Coauthors, 2011: Interannual and decadal sst-forced responses of the west african monsoon. *Atmospheric Science Letters*, **12 (1)**, 67–74.

Rotstayn, L. D., and U. Lohmann, 2002: Tropical rainfall trends and the indirect aerosol effect. *Journal of Climate*, **15 (15)**, 2103–2116.

Salack, S., A. Giannini, M. Diakhaté, A. T. Gaye, and B. Muller, 2014: Oceanic influence on the sub-seasonal to interannual timing and frequency of extreme dry spells over the west african sahel. *Climate dynamics*, **42**, 189–201.

Sanogo, S., A. H. Fink, J. A. Omotosho, A. Ba, R. Redl, and V. Ermert, 2015: Spatio-temporal characteristics of the recent rainfall recovery in west africa. *International Journal of Climatology*, **35 (15)**, 4589–4605.

Sanogo, S., P. Peyrillé, R. Roehrig, F. Guichard, and O. Ouedraogo, 2022: Extreme precipitating events in satellite and rain gauge products over the sahel. *Journal of Climate*, **35 (6)**, 1915–1938.

Shiogama, H., and Coauthors, 2023: Miroc6 large ensemble (miroc6-le): experimental design and initial analyses. *Earth System Dynamics Discussions*, **2023**, 1–28.

Sivakumar, M., 1988: Predicting rainy season potential from the onset of rains in southern sahelian and sudanian climatic zones of west africa. *Agricultural and forest meteorology*, **42 (4)**, 295–305.

Sow, M., R. D. Dixon, M. Diakhaté, F. Guichard, F. Couvreux, and A. T. Gaye, 2025: Contribution from the occurrence and intensity of west days to the west african rainfall variability in cmip6 models. *Geophysical Research Letters*, **52 (21)**, e2024GL110 022.

Sultan, B., S. Janicot, and A. Diedhiou, 2003: The west african monsoon dynamics. part i: Documentation of intraseasonal variability. *Journal of Climate*, **16 (21)**, 3389–3406.

907 Tatebe, H., and Coauthors, 2019: Description and basic evaluation of simulated mean state,
908 internal variability, and climate sensitivity in miroc6. *Geoscientific Model Development*, **12 (7)**,
909 2727–2765.

910 Taylor, C. M., and Coauthors, 2017: Frequency of extreme sahelian storms tripled since 1982 in
911 satellite observations. *Nature*, **544 (7651)**, 475–478.

912 Thorncroft, C. D., H. Nguyen, C. Zhang, and P. Peyrillé, 2011: Annual cycle of the west african
913 monsoon: regional circulations and associated water vapour transport. *Quarterly Journal of the*
914 *Royal Meteorological Society*, **137 (654)**, 129–147.

915 Ting, M., Y. Kushnir, R. Seager, and C. Li, 2009: Forced and internal twentieth-century sst trends
916 in the north atlantic. *Journal of Climate*, **22 (6)**, 1469–1481.

917 Ting, M., Y. Kushnir, R. Seager, and C. Li, 2011: Robust features of atlantic multi-decadal
918 variability and its climate impacts. *Geophysical Research Letters*, **38 (17)**.

919 Villamayor, J., E. Mohino, M. Khodri, J. Mignot, and S. Janicot, 2018: Atlantic control of the late
920 nineteenth-century sahel humid period. *Journal of Climate*, **31 (20)**, 8225–8240.

921 Wane, D., A. Giannini, A. Kaplan, and A. T. Gaye, 2025: An imminent return to drought in the
922 western sahel? *Science Advances*, **11 (34)**, eadu5415.

923 Wilks, D. S., Ed., 2019: *Statistical Methods in the Atmospheric Sciences (Fourth Edition)*. 4th
924 ed., Elsevier, https://doi.org/https://doi.org/10.1016/B978-0-12-815823-4.09994-6, URL https:
925 //www.sciencedirect.com/science/article/pii/B9780128158234099946.

926 WMO, 2009: Guidelines on analysis of extremes in a changing climate in support of informed
927 decisions for adaptation. *World Meteorological Organization*, **1500**, 72.

928 Zhang, J., and Coauthors, 2021: On the connection between amoc and observed land precipitation
929 in northern hemisphere: a comparison of the amoc indicators. *Climate Dynamics*, **56 (1)**, 651–
930 664.

931 Zhang, R., and T. L. Delworth, 2006: Impact of atlantic multidecadal oscillations on india/sahel
932 rainfall and atlantic hurricanes. *Geophysical research letters*, **33 (17)**.

Zhang, R., R. Sutton, G. Danabasoglu, Y.-O. Kwon, R. Marsh, S. G. Yeager, D. E. Amrhein, and C. M. Little, 2019: A review of the role of the atlantic meridional overturning circulation in atlantic multidecadal variability and associated climate impacts. *Reviews of Geophysics*, **57 (2)**, 316–375.

Zhang, S., P. Stier, G. Dagan, and M. Wang, 2022: Anthropogenic aerosols modulated 20th-century sahel rainfall variability via their impacts on north atlantic sea surface temperature. *Geophysical Research Letters*, **49 (1)**, e2021GL095 629.